Double-peaked Balmer Emission Indicating Prompt Accretion Disk Formation in an X-Ray Faint Tidal Disruption Event

Tiara Hung[1], Ryan J. Foley[1], Enrico Ramirez-Ruiz[1,2], Jane L. Dai[2,3], Katie Auchettl[1,2,4,5], Charles D. Kilpatrick[1], Brenna Mockler[1], Jonathan S. Brown[1], David A. Coulter[1], Georgios Dimitriadis[1], Thomas W.-S. Holoien[6], Jamie A. P. Law-Smith[1], Anthony L. Piro[6], Armin Rest[7], César Rojas-Bravo[1], and Matthew R. Siebert[1]

[1] Department of Astronomy and Astrophysics, University of California, Santa Cruz, CA 95064, USA; tiarahung@ucsc.edu
[2] DARK, Niels Bohr Institute, University of Copenhagen, Lyngbyvej 2, DK-2100 Copenhagen, Denmark
[3] Department of Physics, The University of Hong Kong, Pokfulam Road, Hong Kong
[4] School of Physics, The University of Melbourne, Parkville, VIC 3010, Australia
[5] ARC Centre of Excellence for All Sky Astrophysics in 3 Dimensions (ASTRO 3D), Australia
[6] The Observatories of the Carnegie Institution for Science, 813 Santa Barbara Street, Pasadena, CA 91101, USA
[7] Space Telescope Science Institute, Baltimore, MD 21218, USA
Received 2020 March 20; revised 2020 July 17; accepted 2020 August 13; published 2020 October 29

Abstract

We present the multiwavelength analysis of the tidal disruption event (TDE) AT 2018hyz (ASASSN-18zj). From follow-up optical spectroscopy, we detect the first unambiguous case of resolved double-peaked Balmer emission in a TDE. The distinct line profile can be well-modeled by a low eccentricity ($e \approx 0.1$) accretion disk extending out to $\sim 100\, R_p$ and a Gaussian component originating from non-disk clouds, though a bipolar outflow origin cannot be completely ruled out. Our analysis indicates that in AT 2018hyz, disk formation took place promptly after the most-bound debris returned to pericenter, which we estimate to be roughly tens of days before the first detection. Redistribution of angular momentum and mass transport, possibly through shocks, must occur on the observed timescale of about a month to create the large Hα-emitting disk that comprises $\lesssim 5\%$ of the initial stellar mass. With these new insights from AT 2018hyz, we infer that circularization is efficient in at least some, if not all optically bright, X-ray faint TDEs. In these efficiently circularized TDEs, the detection of double-peaked emission depends on the disk inclination angle and the relative strength of the disk contribution to the non-disk component, possibly explaining the diversity seen in the current sample.

Unified Astronomy Thesaurus concepts: Galaxy accretion disks (562); Black hole physics (159); High energy astrophysics (739)

Supporting material: machine-readable table

1. Introduction

When a hapless star approaches a supermassive black hole (SMBH) too closely it will be torn apart by tidal forces (Hills 1975; Rees 1988). After the disruption, a nascent accretion disk is expected to form and produce a luminous flare (Hills 1975; Frank & Rees 1976). These bright transients have been observed at the centers of quiescent galaxies, and evolve distinctly from supernovae, leading to their identification as tidal disruption events (TDEs).

In the past decade, wide-field ground-based optical time domain surveys have discovered tens of TDEs, which affords us the opportunity to study these rare phenomena extensively across the electromagnetic spectrum. Until now, only a small fraction ($\sim 10\%$) of TDEs has been detected with X-ray emission, where the presence of an accretion disk can be confidently established (e.g., Miller et al. 2015; Holoien et al. 2016a; Kara et al. 2018). For the majority of the optically discovered TDEs, there has been no clear proof (Gezari et al. 2012; Holoien et al. 2016b; Hung et al. 2017) that the infalling stellar debris are able to circularize and form an accretion disk (Dai et al. 2013, 2015; Guillochon et al. 2014; Guillochon & Ramirez-Ruiz 2015; Shiokawa et al. 2015; Bonnerot et al. 2016; Gezari et al. 2017). Whether an accretion disk can form promptly following a TDE has long been a debate as alternative mechanisms such as stream–stream collision are thought to be capable of powering the UV/optical emission in an optically

discovered TDE even when disk formation is inefficient (Piran et al. 2015; Bonnerot et al. 2017).

Here we report the telltale evidence of an accretion disk in a nearby TDE called AT 2018hyz (also known as ASASSN-18zj). AT 2018hyz is a TDE first detected on 2018 November 6 with an apparent V-band magnitude of 16.4 by the All-Sky Automated Survey for Supernovae (Shappee et al. 2014). The transient aligns with the nucleus of the galaxy 2MASS J10065085+0141342 at $z = 0.0457$ that is absent of pre-flare nuclear activity. An archival Sloan Digital Sky Survey (SDSS) spectrum of the host galaxy displays strong Balmer absorption lines that are characteristic of an E + A galaxy, a rare subtype of post-starburst galaxies in which TDEs are preferentially discovered (Arcavi et al. 2014; French et al. 2016; Law-Smith et al. 2017; Graur et al. 2018). Following the spectroscopic classification of AT 2018hyz as a TDE (Dong et al. 2018), we triggered photometric and spectroscopic monitoring spanning about a year in time.

The discovery of double-peaked emission features in the spectra of AT 2018hyz is a strong indication of an elliptical accretion disk (Chen et al. 1989; Eracleous et al. 1995) orbiting the SMBH, though alternative scenarios such as a bipolar outflow are not entirely ruled out. Our findings suggest that the infalling debris in TDEs begin forming an accretion disk soon after the most highly bound material falls back. This accretion powers the TDE, which is a sign of the presence of an
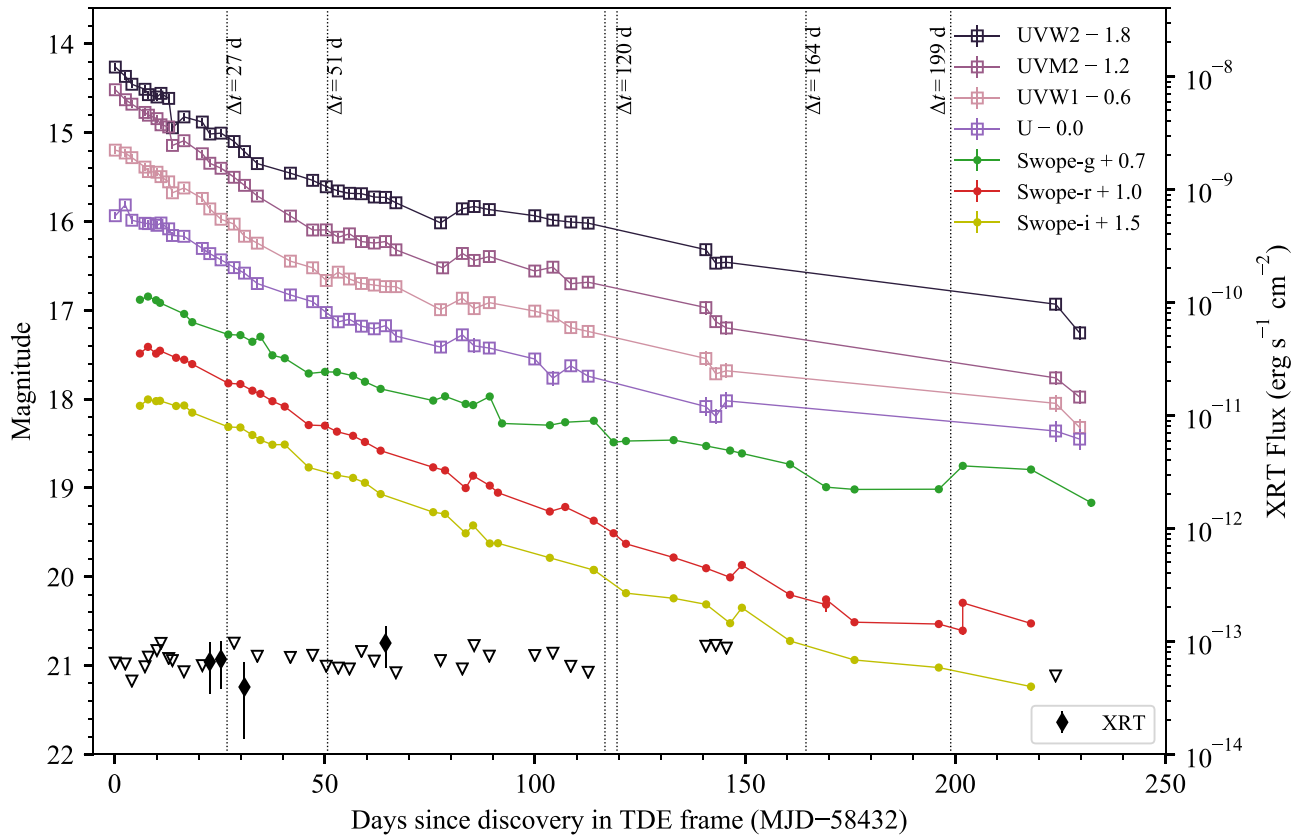
Figure 1. Multiwavelength light curves of AT 2018hyz. The host-galaxy flux has been subtracted from the Swope light curves but not the Swift light curves; however, the contamination in the Swift bands are <5% of the flux. XRT (0.3–10 keV) detections are shown as black solid diamonds with values corresponding to the vertical axis on the the right-hand side. Open black triangles mark the XRT upper limits that corresponds to 3σ. The vertical-dotted lines mark the epochs with spectroscopic observations. A late-time spectrum obtained on $\Delta t = 364$ days is outside of our photometric coverage and thus is not indicated in this figure.

otherwise dormant SMBH and a powerful diagnostic of its properties.

In this paper, we present new insights from the first TDE with well-separated, double-peaked emission line profile with high signal-to-noise ratio (S/N). This paper is structured as follows: we describe the follow-up photometric data obtained by Swift and the Swope Telescope, and optical spectra in Section 2. We detail and present the results of emission line modeling in Section 3. Our discussion and conclusions are presented in Sections 4 and 5, respectively.

2. Observations and Data Reduction

Throughout the paper, we adopt a flat Lambda cold dark matter cosmology with $H_0 = 69.3$ km s^{-1} Mpc^{-1}, $\Omega_m = 0.29$, and $\Omega_\Lambda = 0.71$ measured by the Wilkinson Microwave Anisotropy Probe (Bennett et al. 2013). The time difference (Δt) is expressed in rest-frame time with respect to the first Swift observation, which is close to the peak of the light curve, at MJD 58428. All the data for AT 2018hyz presented here have been corrected for Milky Way foreground extinction assuming a Cardelli extinction curve (Cardelli et al. 1989) with $R_V = 3.1$ and $E(B - V) = 0.0288 \pm 0.0007$ mag (Schlafly & Finkbeiner 2011).

2.1. Photometry

Following the spectroscopic classification of AT 2018hyz as a TDE (Dong et al. 2018), we triggered photometric and spectroscopic monitoring spanning about 1 yr in time (between

2018 and 2019 November). Figure 1 displays the light curves of AT 2018hyz observed by the Ultraviolet Optical Telescope (UVOT; Gehrels et al. 2004; Roming et al. 2005) and simultaneously by the X-ray Telescope (XRT) on board the Neil Gehrels Swift Observatory as well as the Swope telescope at the Las Campanas Observatory. We present the values of these photometry data in Tables A1 and A2. The reduction of data obtained by each instrument is detailed in the following subsections.

2.1.1. Swope Photometry

Optical photometry of AT 2018hyz in *gri* was obtained with the 1 m Swope telescope from 2018 November 16 to 2019 June 16 with a 2–5 day cadence. The images were reduced using the photpipe imaging and photometry pipeline (Rest et al. 2005, 2014). We subtracted the bias and flattened each frame using bias and sky flat images obtained on the same night and in the same instrumental configuration as each AT 2018hyz image. The images were registered and geometric distortion was removed using Two Micron All Sky Survey (2MASS) astrometric standards (Cutri et al. 2003). We measured a S/N-weighted offset of $0.5'' \pm 0.3''$ from all of our Swope images in *gri* bands, confirming that the transient is nuclear as expected for a TDE. Using hotpants (Becker 2015), we subtracted pre-discovery Pan-STARRS1 (PS1) template images (Flewelling et al. 2016) from each Swope *gri* frame. For the *u*-band images, we used SDSS template images (Aihara et al. 2011). We then obtained photometry of AT 2018hyz using a

Table 1
Observing Details of the Optical Spectra of AT 2018hyz

Obs. Date	Phase (days)	Telescope + Instrument	Slit Width	Grism/Grating	Exp Time (s)
2018-12-08	27	Keck I + LRIS	1.0″	600/4000+400/8500	230
2019-01-02	51	Shane + Kast	2.0″	452/3306+300/7500	1800 (blue) 1755 (red)
2019-03-12	117	SOAR + Goodman	1.0″	400 m2	1500
2019-03-15	120	Shane + Kast	2.0″	452/3306+300/7500	2460 (blue) 2400 (red)
2019-05-01	165	Keck I + LRIS	1.0″	600/4000+400/8500	1500 (blue) 1396 (red)
2019-06-06	199	SOAR + Goodman	1.0″	400 m1	1800
2019-11-26	364	Keck I + LRIS	1.0″	600/4000+400/8500	1500 (blue) 1400 (red)

custom-built version of DoPhot (Schechter et al. 1993) and a fixed point-spread function (PSF) in the difference images themselves. The photometry is calibrated using PS1 sources in the same field and transformed into the Swope natural system (Scolnic et al. 2015). The final difference-image photometry of AT 2018hyz is displayed in Figure 1.

2.1.2. UVOT Photometry

We extracted UV light curves from a series of 38 observations obtained with the Swift UVOT using a 5″ circular aperture. Although the observations were made in all six UVOT filters ($UVW2$, $UVM2$, $UVW1$, U, B, and V), we do not include the Swift B- and V-band data in Figure 1 since galaxy light is non-negligible in these bands and host templates cannot be obtained yet. Given that the host galaxy is of an early type that contributes very little of the observed UV light ($u >$ 19.9 mag), we did not attempt host galaxy subtraction for the Swift light curves presented in Figure 1.

2.1.3. XRT Photometry

Simultaneous Swift XRT observations of AT 2018hyz were also obtained, complementing our Swift UVOT observations. All level-one XRT data were analyzed and reduced using the standard filters and screening criteria as suggested in the Swift XRT data reduction guide[8] and using the Swift XRTPIPELINE version 0.13.2 with the most up-to-date calibration files. To quantify the presence of X-ray emission at the position of AT 2018hyz, we used a source region with a radius of 50″ centered on the position of AT 2018hyz and a source-free background region with a radius of 150″ centered at R.A. = $10^h06^m59.^s6$, decl. = $+01°47'56.3''$ (J2000). Since only a fraction of possible AT 2018hyz photons can be captured by the size of the source region, all extracted count rates are corrected for the encircled energy fraction.[9]

In most Swift XRT epochs, we do not detect X-ray emission from AT 2018hyz. In these cases, we derive a 3σ upper limit to the count rate. However, approximately 27, 29, 35, and 70 days after discovery we detect faint X-ray emission arising from the source.

To convert our count rate (both upper limits and detections) into a flux, we assume an absorbed power-law model with a photon index of $\Gamma = 2.7$, which is the best-fitting value for the spectrum extracted from all Swift XRT observations combined. To merge our observations, we used XSELECT version 12.9.1 c, while we used the Swift task XRTPRODUCTS to extract both source and background spectra. Ancillary response

files were created using XRTMKARF, while we used the ready-made response matrix files that are available in the Swift CALDB. This merged spectrum was grouped using the FTOOLS command *grppha* and assumed to have a minimum of 10 counts per energy bin. To model the spectrum we used XSPEC 12.10.1f, χ^2 statistics, and assume a redshifted absorbed power law. Here we assume a column density of 2.59×10^{20} cm^{-2}, which is the Galactic H I column density in the direction of AT 2018hyz (HI4PI Collaboration et al. 2016).

2.2. Optical Spectroscopy

We obtained a total of seven spectroscopic observations with the Kast spectrograph (Miller & Stone 1993) on the Lick Shane telescope, the Goodman spectrograph on the Southern Astrophysical Research (SOAR) Telescope (Clemens et al. 2004), and the Low-Resolution Imaging Spectrometer (LRIS) (Oke et al. 1995) on the Keck I telescope. Detailed instrumental configurations are listed in Table 1. We performed standard spectrum extraction and flux absorption with standard PyRAF[10] routines. Observations of standard stars Feige 34 and BD+284211 were used to determine the relative flux calibration and remove telluric features (Foley et al. 2003; Silverman et al. 2012; Dimitriadis et al. 2019). Examining the $\Delta t = 51$ days spectrum in detail (Figure 2), we see that the B-band telluric absorption that partially overlaps the Hα emission profile is effectively removed through our data reduction process and does not introduce artificial structures in the line shape. All of the spectra have been corrected for Galactic extinction. We calibrated each spectrum's absolute flux by comparing the g-band synthetic photometry of each spectrum to the photometry from Swope imaging data (including host contribution), interpolated to each spectroscopic epoch. We then subtracted the host-galaxy light using the archival SDSS spectrum after accounting for instrumental broadening. The galaxy-subtracted spectra are displayed in Figure 3.

3. Analysis and Results

3.1. Black Hole Mass Estimation with MOSFiT

We estimated the black hole mass using both theoretical modeling and the empirical $M_{bh}-\sigma_*$ relation. We used the tidal disruption model implemented in Modular Open Source Fitter for Transients (MOSFiT; Guillochon et al. 2018; Mockler et al. 2019), which assumes that the bolometric luminosity from the flare approximately follows the mass fallback rates from hydrodynamical simulations and translates it into bolometric flux assuming a constant efficiency parameter (the fallback rates used are from Guillochon & Ramirez-Ruiz 2013). While

---
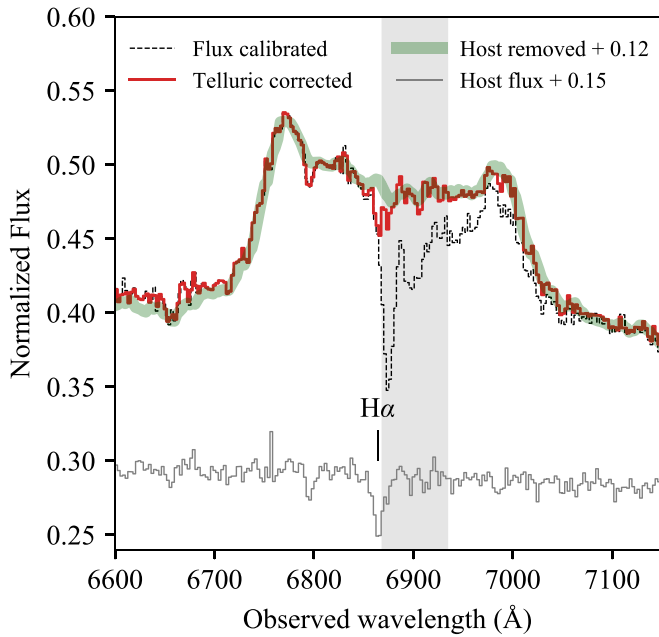
Figure 2. The Hα profile on $\Delta t = 51$ before (black-dashed line) and after (red curve) telluric absorption. The host spectrum from SDSS is plotted as thin gray line. The final host-subtracted spectrum smoothed by a boxcar of 5 Å used in the fitting (see Section 3.4) is shown as the thick green line. The host spectrum and the host-subtracted spectrum have been offset by a constant as indicated in the legend. The gray band marks the region that is affected by the *B*-band telluric absorption.

we do not yet have simulations that show the formation and evolution of TDE disks from realistic debris streams and their resultant light curves, this simple approximation works well to model observed TDE light curves. The model also allows for the possibility that part of the luminosity is originating from stream collisions. After converting the fallback rate to luminosity, the model takes the bolometric flux and reprocesses it using a blackbody photosphere to match our observed flux. The model assumes the photosphere evolves as a power law of the mass fallback rate. This requires the photosphere to grow with the mass fallback rate, but allows significant freedom given the range in allowed power-law exponents and constants. In Jiang et al. (2016) the photosphere radius in their simulations of TDE outflows was fit well by a similar power-law relationship ($R_{\rm phot} \propto L^{\xi}$). As shown in Figure 5, the MOSFiT photosphere matches very well with the photosphere calculated from blackbody measurements that are agnostic to the MOSFiT TDE model.

Possible time delay in the onset of accretion due to either inefficient circularization or the viscous processes in the disk is accounted for in this model using a *viscous time* ($T_{\rm viscous}$) parameter, which we derive to be smaller than the peak timescale. We simultaneously fit all extinction corrected UV and host-subtracted optical photometry in Figure 1 with MOSFiT while prohibiting the peak luminosity to exceed the Eddington limit $L_{\rm Edd}$. This constraint is in agreement with the observations, where most of the TDEs seem to be Eddington capped (Blanchard et al. 2017; Hung et al. 2017; Wevers et al. 2017) at the peak of their light curves. The MOSFiT TDE model has eight parameters listed in Table 1 of Mockler et al. (2019). The best-fit values from the MOSFiT run for this event are presented in Table 2.

We derived a black hole mass of $\log_{10}(M_{\rm bh}/M_{\odot}) = 6.55^{+0.17}_{-0.13}$ with a systematic error of 0.2 dex. In this luminosity range, MOSFiT determines the light-curve peak to occur at MJD 58424^{+6}_{-4}, about 36 days after the most-bound debris falls back. The stellar velocity dispersion measured from the SDSS spectrum is below the SDSS spectral resolution of 70 km s^{-1}. According to the $M_{\rm bh}$–σ_* (McConnell & Ma 2013) relation, this corresponds to an upper limit of $10^{5.7}\,M_{\odot}$ on the black hole mass, with an intrinsic scatter of ∼0.4 dex and a measurement error of 0.2 dex. Such a small black hole mass would indicate a peak luminosity of $\approx 4 L_{\rm Edd}$ that violates our Eddington-limited constraint in MOSFiT. However, if we use the Xiao et al. (2011) $M_{\rm bh}$–σ_* relation, which was derived with a larger fraction of low-mass black holes ($M_{\rm bh} < 10^7\,M_{\odot}$) than the McConnell & Ma (2013) relation (Figure 4), we find a black hole mass of $10^{6.2}\,M_{\odot}$ with an intrinsic scatter of ∼0.5 dex, which is in better agreement with the best-fit $M_{\rm bh}$ estimated by MOSFiT. It is also noteworthy that the empirical $M_{\rm bh}$–σ_* relation is not well constrained for the low-mass end. High-resolution spectroscopy of the host galaxy after AT 2018hyz has faded is required for a more precise determination of the stellar dispersion and hence the black hole mass. For consistency when comparing with previously found Eddington-capped events, we adopt the black hole mass of $3.5 \times 10^6\,M_{\odot}$ from MOSFit throughout the paper. We also adopt this value when converting distance measurements in units of gravitational radius in our analysis.

3.2. Temperature, Photospheric Radius, and Luminosity

The light curves of AT 2018hyz are displayed in Figure 1. Analysis of the Swift XRT observations revealed marginal soft X-ray emission (0.3–10 keV) with $L_X = 2.8 \times 10^{41}$ erg s^{-1}, which is almost three orders of magnitude fainter than the UV–optical emission.

We measured the temperature and the luminosity by assuming that the UV and optical emission is characterized by a blackbody spectrum on the epochs of Swift observations. For the first three Swift epochs (MJD < 58439) that are out of the temporal coverage of Swope, we constructed the spectral energy distribution (SED) using only the *UVW2*, *UVW1*, *UVM2*, and *U* filters. For the later Swift epochs, we included the optical (*g*, *r*, and *i*) photometry in the SEDs by interpolating the Swope light curves to these epochs. By modeling the SEDs with a single-temperature blackbody, we find that the light curve is well described by a single-temperature blackbody ($T_{\rm bb} = 18,000 \pm 2000$ K) whose temperature evolves only mildly with time.

We measured the luminosity at each Swift epoch by integrating the best-fit blackbody spectrum of each UV–optical SED. We also calculated the emitting radius of the blackbody with the Stefan–Boltzmann law and plotted the evolution of the blackbody radius in the left panel of Figure 5. The size of the blackbody radius is tens of times larger than the pericenter distance of the disrupted star,

$$R_{\rm p} \approx 7 \times 10^{12} \left(\frac{M_{\rm bh}}{10^6 M_{\odot}}\right)^{1/3} \left(\frac{R_{\star}}{R_{\odot}}\right) \left(\frac{M_{\star}}{M_{\odot}}\right)^{-1/3} {\rm cm}, \quad (1)$$

and shrinks with time. The evolution of the blackbody temperature and radius is similar to that of previously studied TDEs (e.g., Hung et al. 2017; Holoien et al. 2019).

Our follow-up photometric observations of AT 2018hyz were made after the peak of the UV/optical light curve.
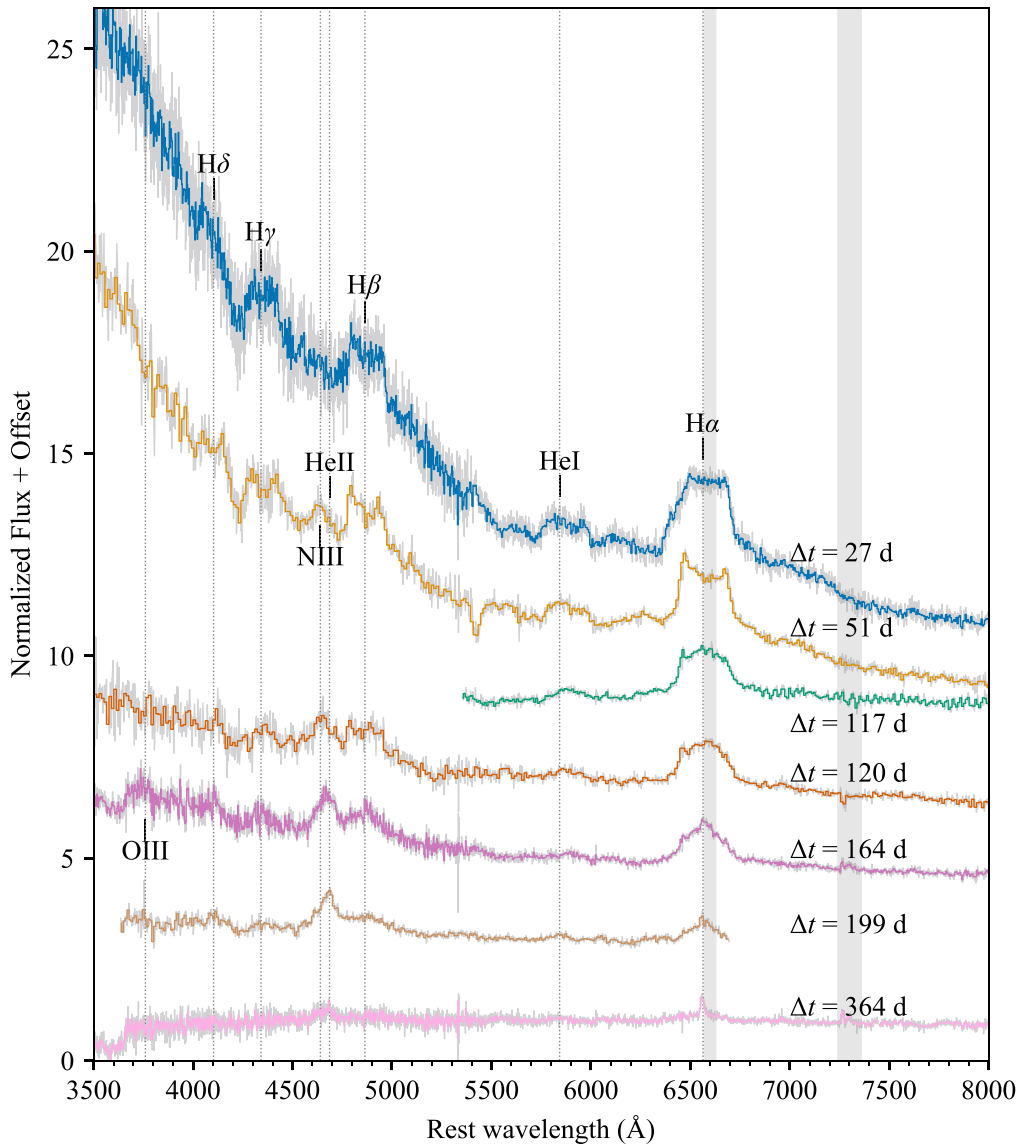
Figure 3. Observed spectroscopic sequence of AT 2018hyz with host-galaxy light subtracted. The gray curves are the observed spectra while the colored solid curves are the observed spectra smoothed by 4.5 Å. TDE emission lines are indicated by vertical gray-dotted lines with labels marked. The gray-shaded regions indicate the location of telluric absorption features that have been corrected using standard-star observations. As AT 2018hyz evolves, the He I emission diminishes, while the Bowen emission lines (N III and He II) become stronger. The Hα emission line evolves from a flat-topped shape in the first spectrum to double-peaked in the second to single peaked in the last spectrum on a timescale of months is unseen in other TDEs. The strong absorption feature on day 51 at around 5430 Å is likely the Na I D blueshifted by ∼0.08c.

However, from the ASASSN data, the peak of the g-band light curve is estimated to occur around MJD = 58429 (Gomez et al. 2020), which is very close to our first Swift observation on MJD = 58432. We thus quote the luminosity measured from the first Swift epoch and estimate a radiated luminosity of $\gtrsim 2.5 \times 10^{44}$ erg s^{-1} at peak, which translates to an Eddington ratio of 0.6 for $M_{\rm bh} = 3.5 \times 10^6 M_\odot$. This places AT 2018hyz among one of a handful of TDEs radiating near the Eddington limit, such as ASASSN-14li and PS16dtm (Blanchard et al. 2017; Brown et al. 2017), while the majority of previously studied TDEs (mostly X-ray faint) are found to radiate at ∼10% level of the Eddington luminosity near peak (Blanchard et al. 2017; Hung et al. 2017).

At such high luminosities, radiation pressure is expected to be large enough to increase the disk thickness and produce optically thick winds (Shakura & Sunyaev 1973; King & Pounds 2003; Ohsuga et al. 2005). Stream–stream collisions can also unbind a large fraction of shocked gas at the origin of disk formation, resulting in a collision-induced outflow (Jiang et al. 2016; Lu & Bonnerot 2020). These naturally give rise to an extended reprocessing envelope covering the X-ray emission site from a large solid angle (Loeb & Ulmer 1997; Lodato & Rossi 2011; Dai et al. 2018). Similar to what is observed in other optically discovered TDEs, the luminosity evolution of AT 2018hyz closely follows the classical mass fallback rate ($t^{-5/3}$) of the debris streams (Holoien et al. 2014; Auchettl et al. 2017; Blagorodnova et al. 2017; Hung et al. 2017; Holoien et al. 2019; Mockler et al. 2019; van Velzen et al. 2019; Gomez et al. 2020). If these TDE flares are indeed powered by accretion onto the SMBH, this would require the disk to form promptly. Our analysis indicates that in AT 2018hyz, disk formation took place soon after the most-bound debris returned to pericenter, which we estimate to be about tens of days before the first detection (see MOSFiT results in Section 3.1). However, as in all other
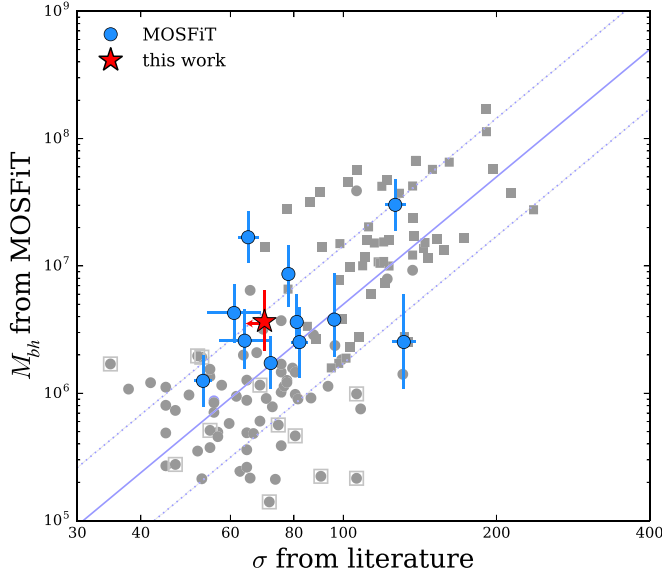
Figure 4. M_{bh}–σ_* for host galaxies of TDEs (blue circles) and galaxies with black hole masses measured by Xiao et al. (2011) (gray symbols; see shape notation in their paper). The derived black hole mass from this work is shown by the red star. Black hole masses estimated from MOSFiT for TDEs are adopted from Mockler et al. (2019) and Leloudas et al. (2019), and include a compilation of velocity dispersion across references of individual objects. The solid line marks the M_{bh}–σ_* in Xiao et al. (2011), where the dotted lines show the intrinsic scatter of 0.46 dex.

Table 2
Best-fit Parameters from MOSFiT

Parameter[a]	Value	Sys. Error[b]
$t_{\text{first fallback}}$ (days)[c]	-43^{+8}_{-9}	15
$\log_{10} R_{ph0}$	$0.70^{+0.03}_{-0.03}$	0.4
$\log_{10} T_{\text{viscous}}$ (days)	$-1.2^{+1.1}_{-1.3}$	0.1
l_{photo}	$0.65^{+0.04}_{-0.03}$	0.2
β	$1.7^{+0.1}_{-0.2}$	0.35
$\log_{10} M_h$ ($M_\odot$)	$6.55^{+0.17}_{-0.13}$	0.2
$\log_{10}\epsilon$	$-2.49^{+0.14}_{-0.05}$	0.68
M_* ($M_\odot$)	$1.0^{+0.1}_{-0.1}$	0.66

Notes.
[a] See Mockler et al. (2019) for detailed parameter definition.
[b] The systematic errors for this model were calculated by allowing the stellar mass–radius relation in the model to vary over a wide range of ages and metallicity combinations (using the MESA Isochrones and Stellar Tracks models—Paxton et al. 2011, 2013, 2015; Choi et al. 2016; Dotter 2016). Allowing this relation to vary approximates the changes in stellar structure expected for stars of different ages and metallicities, which is likely the largest source of systematic error in the MOSFiT TDE model (see Mockler et al. 2019). Other potential sources of error not currently included in the error estimates include the spin of the star and the black hole, and very deep impact parameters. The magnitude of the effects of stellar or black hole spin will be less than the effects of the uncertainty in the stellar structure unless the star is spinning close to its breakup speed ($>0.2\Omega_{\text{breakup}}$ Golightly et al. 2019), or the impact parameter is very high ($\beta > 6$ Gafton & Rosswog 2019). Most stars will not reach spins of these speeds (Bouvier 2013), and the number of disruptions at a given impact parameter is expected to scale approximately with β^{-1} (Rees 1988), making disruptions at high impact parameters uncommon.
[c] Days relative to the first Swift detection (MJD = 58432).

(This table is available in machine-readable form.)

events, the presence of an accretion disk has not been able to be discerned directly since the disk is likely hidden from our view due to orientation effects (Dai et al. 2018).

3.3. Spectroscopic Features

The most notable feature in the spectra of AT 2018hyz is the double-peaked structure in the Hα emission on day 51, which has two distinct peaks being displaced by 9320 km s^{-1}, with the blue peak being stronger than the red one (Figure 6). As will be detailed in the next section, the Hα emission from day 51 to day 164 can be decomposed into disk and Gaussian components. On the other hand, the Hα emission in the first spectrum, obtained on day 27 seems to lack an obvious double-peaked feature, and instead the entire line is characterized by a broad (FWHM ≈ 13,500 km s^{-1}) flat-topped shape. This line profile is similar to that of the TDE AT 2018zr (PS18kh) and may arise from an elliptical disk with a low inclination angle (Holoien et al. 2019) or an expanding spherical outflow (Hung et al. 2019). We also note that the N III+He II emission, which is strongly detected in later epochs, has yet to emerge at $\Delta t = 27$ days. On the other hand, the low-ionization He I $\lambda 5876$ emission is strongest in the first spectrum.

A strong absorption feature at 5430 Å is only observed in the day-51 spectrum but not in the other epochs. We identify it as Na I D blueshifted by 23,600 km s^{-1} similar to blueshifted absorption features detached from their rest wavelengths that have been observed in other TDEs (e.g., Hung et al. 2019). We have also considered a highly blueshifted He I $\lambda 5876$ absorption to be responsible for this absorption feature. However, this possibility is ruled out since we do not detect blueshifted absorption from He I $\lambda 3889$, which is expected to be even stronger based on photoionization.

3.4. Fitting Hα Emission with the Elliptical-disk Model

Following tidal disruption, the infalling material does not produce an TDE flare immediately. First material must circularize and form an accretion torus. There is no direct evidence supporting that the luminosity of a TDE follows the debris fallback rate that is not known a priori. This assumption, however, if true, would suggest that debris circularization must occur relatively quickly (Guillochon & Ramirez-Ruiz 2015; Mockler et al. 2019). The bound orbits are very eccentric and the orbital semimajor axis of the most tightly bound debris is

$$a \approx 10^3 \left(\frac{M_{bh}}{10^6 M_\odot}\right)^{-1/3} \left(\frac{R_*}{R_\odot}\right) \left(\frac{M_*}{M_\odot}\right)^{-2/3} R_g, \qquad (2)$$

where $R_g \approx 1.5 \times 10^{11}$ $(M_{bh}/10^6 M_\odot)$ cm is the gravitational radius. If the gaseous debris suffered no internal dissipation, it would form a highly elliptical disk with a large spread in apocentric distances between the most- and least-bound orbits. After pericenter passage, the infalling gas is on orbits that can interact with the infalling streams (Ramirez-Ruiz & Rosswog 2009; Dai et al. 2013, 2015; Hayasaki et al. 2013; Guillochon et al. 2014; Guillochon & Ramirez-Ruiz 2015; Shiokawa et al. 2015; Bonnerot et al. 2016; Sądowski et al. 2016; Gezari et al. 2017; Bonnerot & Lu 2020), giving rise to angular momentum redistributing shocks. The debris raining down would then be able to settle into a disk structure. Motivated by the predicted debris stream evolution, we use the elliptical-disk model from Eracleous et al. (1995) to fit the Hα emission in our spectra. We note that Liu et al. (2017) adapted this elliptical-disk model for TDEs by further assuming that the disk size and orientation are determined by the dynamics of the intersecting debris streams.
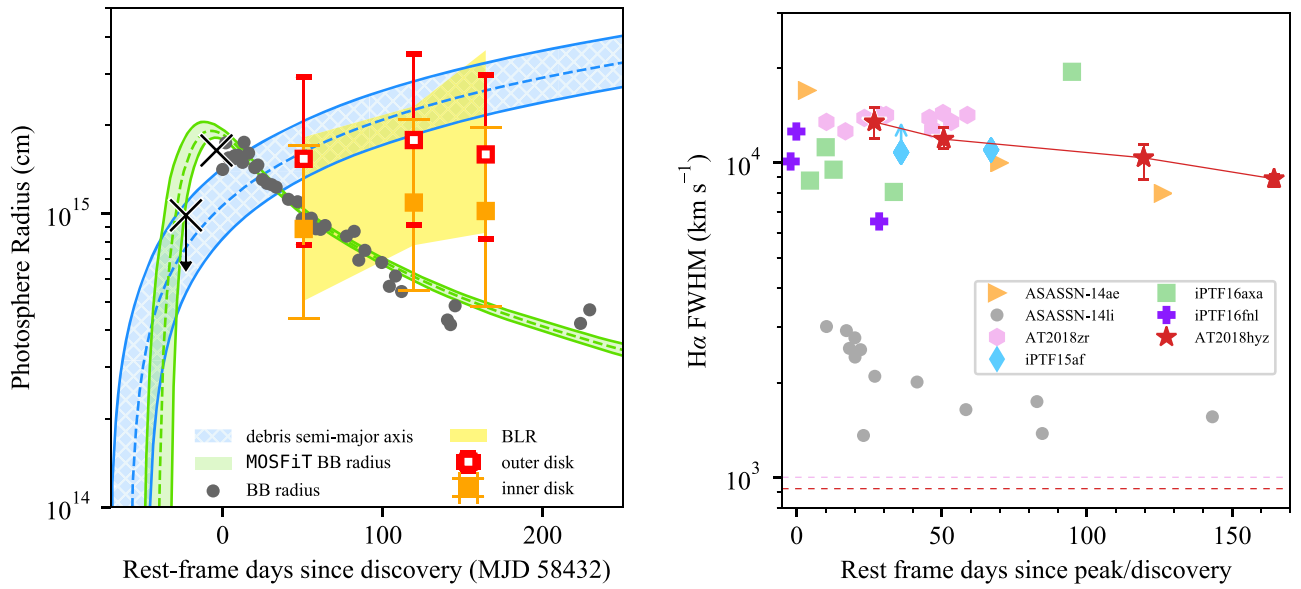
Figure 5. Left: evolution of blackbody radius for AT 2018hyz. The black circles mark the photospheric radius estimated from Swift photometry. The orange and red squares indicate the size of the semimajor axis of the inner and outer part of the best-fitting elliptical disk to our spectral observations, where the error bars mark the 1σ error. The broad-line region (BLR), which corresponds to the velocity width (σ_g) of the Gaussian component seen in our spectra, is shaded in yellow. The blue band marks the semimajor axis of the orbits of the returning stellar debris, which is approximated by Kepler's third law assuming the energy distribution of the gas is frozen in at the time of disruption (see Equation (9) in Guillochon et al. 2014). The green-shaded area shows the photospheric radius from the MOSFiT fit. Both the blue and green bands are bounded by a 1σ statistical error. The black crosses correspond to ASASSN observations in V-band reported on the Transient Name Server https://wis-tns.weizmann.ac.il/object/2018hyz, assuming that the underlying emission is a single-temperature blackbody of $T_{bb} = 18,000$ K. Right: evolution of Hα FWHM for a sample of TDEs. Except for ASASSN-14li, all other TDEs have remarkably similar FWHM of around 10^4 km s^{-1} at early times. The error bars of AT 2018hyz denote the 1σ uncertainty. Double-peaked signatures like the one seen for AT 2018hyz would be hard to identify if they were blended with the broad Gaussian emission lines in these TDEs. The dashed lines show the FWHM of the narrow Hα component observed in AT 2018hyz ($\Delta t = 364$ days) and AT 2018zr ($\Delta t = 169$ days) at late times.

Here we choose to use the original Eracleous et al. (1995) prescription to remain agnostic to the mechanism(s) setting the extent of the elliptical disk.

We first fit the Hα emission in the 51 day spectrum, which has the most prominent double-peaked feature, with an elliptical-disk model. The line profile produced by an elliptical geometrically thin, optically thick relativistic Keplerian disk has been formulated by Eracleous et al. (1995). We constructed the model line profile by computing the line flux, F_X, in their Equation (7) at each velocity/frequency grid, X, with numerical integration after specifying seven parameters. The seven elliptical-disk parameters are the power-law dependence of the emissivity profile q (scales as ξ^{-q}), inner (ξ_1) and outer radii (ξ_2), inclination i, intrinsic broadening parameter σ_{disk}, eccentricity e, and azimuthal angle in the plane of the disk ϕ. The inner and outer radii are defined as the pericenter distance of the inner and outer ellipses expressed in units of gravitational radius (R_g). The inclination is defined such that $i = 0$ when the disk is viewed face-on. The disk orientation angle (ϕ) is measured with respect to the line of sight of the observer, where $\phi = 0$ when the apocenter aligns with the observer. While the seven parameters determine the line shape, the overall normalization is set by the product of emissivity and black hole mass ($\epsilon_0 M^2$). However, as mentioned in Chen et al. (1989), this does not allow us to estimate either parameter since the model expresses radius in dimensionless terms.

The dependence of the elliptical-disk parameters on the computed line shape is nontrivial. Despite this, certain trends can be observed if we vary one parameter at a time as shown in Figure 3 in Eracleous et al. (1995) and Figure 17 in Strateva et al. (2003). For example, the emission line broadens as the

separation between the two peaks becomes larger when we increase the inclination angle (from face-on to edge-on). As the outer disk (ξ_2) increases, the contribution from slow-moving material becomes stronger, and thus the line width narrows. In contrast, the smaller the inner disk radius (ξ_1) is, the broader the emission line is and the more pronounced the Doppler boosting is such that the blue peak becomes noticeably stronger relative to the red peak. Varying the orientation angle of the disk (ϕ) also changes the relative strength of the two peaks, and so in some cases the red peak can be seen stronger than the blue peak. Increasing the local broadening (σ_{disk}) smooths the peaks of the line profile.

We attempted fitting the observed Hα emission line profile on day 51 with the elliptical-disk model by minimizing χ^2 in the following parameter space: $1 < q < 4$, $100 < \sigma_{disk} < 1000$ km s^{-1}, $0 \leqslant i < \frac{\pi}{2}$ rad, $0 < e < 1$, $0 \leqslant \phi < 2\pi$ rad, $100 < \xi_1 < 3000$ R_g, and $100 < \xi_2 < 10,000$ R_g. We show the model parameters and the ranges of the flat priors in Table 3. We noticed that the best-fitting disk-only model does not capture the sharp peaks around the edges of the profile, but instead has broader peaks in order to match the high central flux. Alternatively, if we attempt to fit only the edges of the profile by excluding the central data (with $|\Delta v| < 3000$ km s^{-1}), the best-fitting model, which is tabulated in Table 4, then lacks the flux seen at the center of the line profile (shown as the green line in Figure 6). Clearly, a second component is needed to account for the central flux.

In order to match the full line profile, we add a Gaussian component to the disk model. We smoothed the data of the Hα emission with a boxcar function with a length of $\sim$5 Å to erase fine structures that cannot be captured by the emission-line
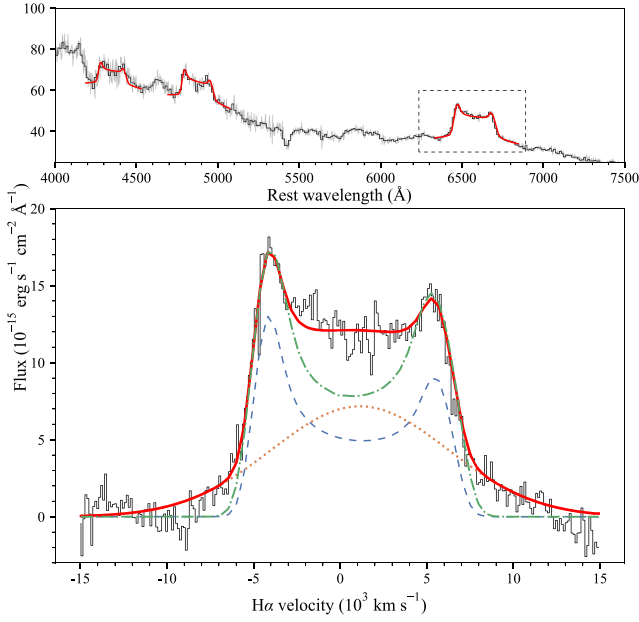
Figure 6. $\Delta t = 51$ day spectrum zoomed in on the Hα emission line profile and best-fitting model. The top and bottom panels are of the same flux scale. The black histogram in the top panel shows the binned spectrum, while the gray curve marks the original spectrum with host light subtracted. The red curves show the best-fitting two-component model derived from the Hα profile (dashed box; enlarged in lower panel), rescaled by 1, 0.82, and 0.62 and shifted to the rest wavelength of Hα, Hβ, and Hγ emission, respectively, on top of the local continuum. The local continuum is estimated by linearly interpolating the regions bracketing each emission line. The black curve in the lower panel shows the zoom-in view of the continuum-subtracted Hα line profile. The solid red curve is the best-fitting two-component (disk + Gaussian) model with the parameters indicated in Table 4. The two components are shown separately by the orange-dotted line (Gaussian) and in the blue-dashed line (disk). The green line shows the best-fitting model with only the disk component by omitting the center part of the line flux. It is clear that the disk-only model cannot reproduce the all flux near zero velocity.

Table 3
Fitting Parameters

| Parameter	Notation	Unit	Min	Max
Elliptical-disk component				
Emissivity power-law exponent	q		1	4
Inner radius	ξ_1	R_g	10^2	3×10^3
Outer radius	ξ_2	R_g	10^2	10^4
Inclination (rad)	i	rad	0	$\frac{\pi}{2}$
Intrinsic broadening parameter	σ_{disk}	km s^{-1}	10^2	10^3
Eccentricity	e		0	1
Orientation angle	ϕ	rad	0	2π
Gaussian component				
Amplitude	A	Normalized flux	0	1
Velocity offset	μ_0	km s^{-1}	-3×10^3	3×10^3
Gaussian width	σ_g	km s^{-1}	0	2×10^4

model. Using the `emcee` package (Foreman-Mackey et al. 2013), we sampled the posterior distribution of a total of 10 parameters (the seven disk parameters listed above and an additional three parameters that describe the Gaussian: amplitude, center (μ_0; velocity offset from the systemic velocity

of the host galaxy), and width (σ_g; standard deviation) using flat priors over the aforementioned ranges for the disk parameters and over the following ranges for the Gaussian component: $-3000 < \mu_0 < 3000$ km s^{-1} and $0 < \sigma_g < 20,000$ km s^{-1} (Table 3). The model parameter σ_g can be translated to the FWHM of the Gaussian profile via the relation FWHM $= 2\sqrt{2\log 2}\,\sigma_g$. We normalized our flux to range between 0 and 1 and use this same range as the flat prior for the amplitude of the Gaussian. The posterior distributions of the model parameters are shown in Figure 7. The MCMC approach provides a more general description of the model parameters, instead of forcing them to be Gaussian distributed as in traditional fitting methods. In addition, we can also visualize the correlation between different parameters in the joint distributions, such as that between i, ξ_1, and ξ_2, which intricately control the overall width of the disk profile. From this, we derived the parameters for the two-component (disk-plus-Gaussian) model and present the derived parameters in Table 4 and compare the best-fitting model to the spectrum in Figure 6. The blue Hα emission peak being relatively stronger than the red peak can be explained by Doppler boosting in the scheme of an axisymmetric accretion disk, though we note that the relative strength of the two peaks is orientation-dependent in elliptical disks.

To summarize, the day-51 spectrum is best described by two distinct spectral components: a non-disk broad Gaussian component with a centroid velocity close to the systemic velocity of the host (similar to that observed in all other TDEs) and a prominent disk/double-peak component (see Figure 6). The Hα line profile in the day-120 and day-164 spectra still shows a double-horned shape, despite being less prominent relative to the Gaussian component than that in the $\Delta t = 51$ days spectrum. However, because the disk parameters are the most constrained by the shape and strength of the double-peaked structure, the dominance of the Gaussian component at later stages means that performing a fully independent fit for these epochs would result in loosely constrained model parameters. Therefore, when fitting the Hα emission with the MCMC in the later two epochs, we fixed the surface emissivity to the best-fit value ($q = 2$) from day 51. This value is between the emissivity index of local dissipation of gravitational energy ($q = 1.5$, such as seen in cataclysmic variable disks; Horne & Saar 1991) and that of a disk illuminated by an isotropic ionizing source ($q = 3$; Chen et al. 1989; Wilkins & Fabian 2012). The rest of the parameters were set to have the same flat priors as above. Although the disk parameters are less constrained in the two later epochs (Table 4), the inclination angle and inner/outer disk radii are still consistent with the fit for the day-51 spectrum. We find a decreased relative disk contribution to the flux over time. On day 51, the integrated flux of the disk is comparable to the Gaussian component but only 28% of the Gaussian component in the day-120 spectrum. We plot the size of the elliptical disk and the BLR (derived from the Gaussian component) in all three epochs along with the photospheric radius derived from Swift photometry as shown in the left panel of Figure 5. In the right panel of Figure 5, we show the evolution of the best-fit FWHM of the Gaussian component compared to the evolution of Hα width in other TDEs. The width and the evolution of this Gaussian component are similar to that seen in other optical TDEs (Hung et al. 2017).

We did not attempt fitting the first spectrum (day 27) since the flat-topped line shape without visible blue and redshifted
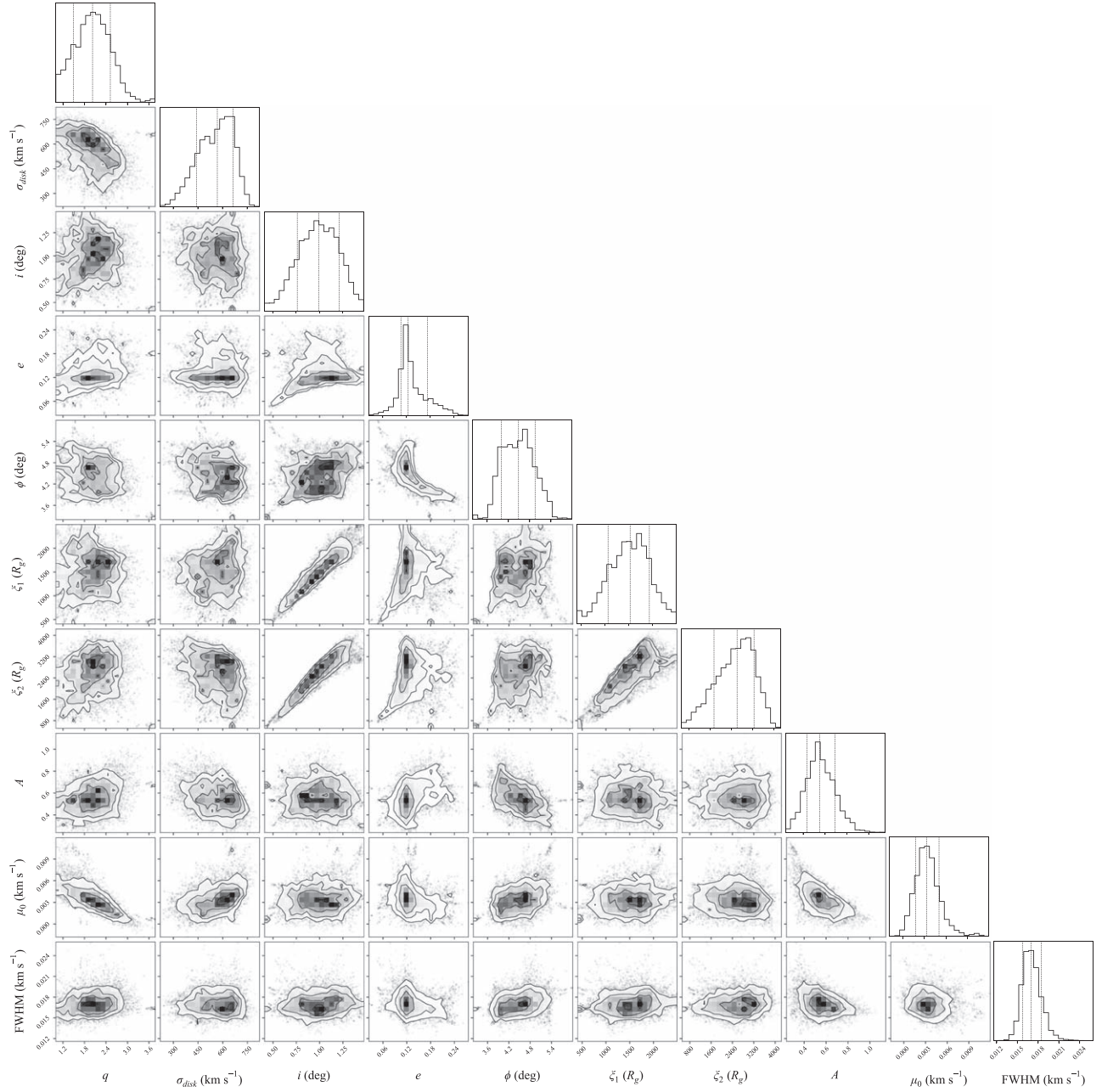
Figure 7. Posterior distributions of parameters for the two-component elliptical-disk + Gaussian model. The histograms at the top of each column show the marginalized posterior distribution for each parameter. The vertical-dashed lines mark the quoted values in Table 4, which correspond to the 16th, 50th, and 84th percentiles, respectively. For each parameter pair, the joint posterior distribution is shown as a 2D histogram where the contours correspond to the 16th, 50th, and 84th percentiles.

Table 4
Elliptical-disk Model Constraints Derived from the Hα Emission Line Profile

Obs. Date	Phase	Disk							Gaussian	
		q	σ_{disk} (km s^{-1})	i (deg)	e	ϕ (deg)	ξ_1 (R_g)	ξ_2 (R_g)	μ_0 (km s^{-1})	FWHM (km s^{-1})
	(days)									
2019-01-02	51	2.9 ± 0.1	640 ± 70	52^{+13}_{-16}	$0.14^{+0.06}_{-0.04}$	242^{+27}_{-19}	1200^{+400}_{-500}	2700^{+900}_{-1200}	...	...
2019-01-02	51	2.0 ± 0.5	570^{+90}_{-130}	57 ± 13	$0.13^{+0.05}_{-0.02}$	257^{+27}_{-28}	1500^{+400}_{-500}	2600^{+600}_{-900}	990^{+520}_{-450}	11900^{+1050}_{-800}
2019-03-15	120	2.0	450^{+250}_{-170}	68^{+11}_{-18}	$0.10^{+0.1}_{-0.06}$	229^{+91}_{-78}	1900^{+800}_{-700}	3100^{+900}_{-1000}	660^{+360}_{-300}	10380^{+1070}_{-1540}
2019-05-01	165	2.0	370^{+180}_{-110}	65^{+13}_{-18}	$0.09^{+0.1}_{-0.04}$	222^{+77}_{-25}	1800^{+500}_{-600}	2800^{+700}_{-1000}	140^{+90}_{-80}	8900^{+300}_{-500}

Note. The Hα emission line on 2019 January 2 was fit with a disk-only model (first line) and a disk + Gaussian model (second line). For all other epochs, results from only the disk + Gaussian model are shown. The uncertainties listed are the 16th and 84th percentile of the marginal posterior distribution for each parameter.

peaks leaves our model parameters poorly constrained. However, it is likely that the Hα emission from the $\Delta t = 27$ days spectrum also consists of the same disk and the Gaussian component given their FWHMs do not vary significantly. The double-peaked disk feature on $\Delta t = 27$ days may be buried due to a relatively weaker disk contribution relatively to the Gaussian component. We did not fit the Hα in the $\Delta t = 117$ days spectrum because of its proximity in time to the $\Delta t = 120$ days spectrum. As can be seen in Figure 3, the line shape barely changed during this 3-day period. We also omitted fitting the $\Delta t = 199$ days spectrum because the spectral coverage does not extend redward enough to cover the entire Hα emission. The Hα in the late-time spectrum became a narrow emission line and thus we did not attempt fitting it with an elliptical accretion disk.

From our analysis, we find that a quasi-circular disk ($e \approx 0.1$) with a mean semimajor axis ($a \equiv \frac{\xi_1 + \xi_2}{2(1 - e)}$) of $2400 R_g$ ($\approx 1.2 \times 10^{15}$ cm) is responsible for the double-peaked Hα emission in AT 2018hyz. Assuming Keplerian motion, the velocity separation of the two Hα peaks (V_{obs}) at $\Delta t = 51$ days corresponds to a radius of $R / R_g = \left(\frac{2c \sin i}{V_{\mathrm{obs}}} \right)^2 = 2900$, which is consistent with the results from our model fitting.

Although the central part of the Hα emission overlaps with the telluric B-band, we were able to recover a smooth emission profile after correcting for the telluric absorption (Figure 2). As a sanity check, we note that the other Balmer lines (Hβ and Hγ) observed at the same time (day 51) also have the same double-peaked line profile. Both Hβ and Hγ can be successfully described by the same disk + Gaussian model (see Figure 6) rescaled and laid on top of a local continuum, lending further support for the realness of the double-peaked emission. As shown by Short et al. (2020), the velocity profiles of Hα and Hβ of AT 2018hyz are broadly consistent throughout the first 5 months. Therefore, the scaling factor derived for the Hβ emission is directly measuring the Balmer decrement (Hα/ Hβ ≈ 1.2). The flat Balmer decrement (relative to the typical case B ratio of 3 for active galactic nuclei (AGNs)) suggests that the production of the Balmer emission is dominated by collisional excitation rather than photoionization at the time of the observation. In an independent work on AT 2018hyz, Short et al. (2020) also derived a Hα/Hβ of 1.5 and pointed out that such a ratio can be achieved in the outer optically thin part of a cataclysmic variable disk (Williams 1980). However, the same mechanism that produces the flat Balmer decrement cannot explain the appearance of He I or He II.

4. Discussion

4.1. Alternative Origin for the Double-peaked Line Profile

Accretion disk emission is not the only model for double-peaked emitters. In a TDE environment, another plausible scenario that may result in a double-peaked line profile is the emission from a bipolar outflow. If the redshifted wind component receding from us is not obstructed from our line of sight, one can possibly observe double-peaked emission line profiles. This scenario cannot be completely ruled out even though radio emission from AT 2018hyz was not detected (Horesh et al. 2018). The strength of the radio signal also depends on the density of the circumnuclear gas and therefore TDEs with winds do not necessarily produce strong radio emission (Alexander et al. 2016). From the current TDE

sample, there is no association between radio-detected events and the appearance of double-peaked emission lines.

Nevertheless, it is still unclear whether TDEs can produce outflows with the required geometry, density, and velocity to explain the Hα line profile seen in AT 2018hyz, especially if prompt disk formation has not happened in this event. Simulations have shown that stream–stream collisions in TDEs tend to produce winds that are more or less spherical rather than bipolar (e.g., Jiang et al. 2016). Assuming an accretion origin for the TDE light, Roth & Kasen (2018) showed that a spherical wind can give rise to an asymmetrical flat-topped line profile, similar to that observed in AT 2018zr (Hung et al. 2019). Winds driven by the radiation pressure in super-Eddington disks can produce winds that look bipolar when viewed close to the polar axis. However, such winds are optically thick, therefore are more likely to result in P Cygni features or an asymmetrically broadened/flat-topped emission line.

Given all the evidence, we find the bipolar outflow model less appealing. On the other hand, the disk-plus-Gaussian model provides an excellent fit to the data with model parameters that are physically reasonable. Given current observational evidence, a Keplerian accretion disk is more likely to be responsible for producing the observed double-peaked Hα emission in AT 2018hyz.

4.2. Angular Momentum

Assuming the disrupted star was initially on a parabolic orbit, the total angular momentum of the star at pericenter (R_p) is $\ell_\star = M_\star \sqrt{2GM_{\mathrm{bh}} R_p}$. For the stellar debris to settle into a circular disk, the bulk of the mass must fall in a disk with a radius of $\sim 2R_p$ according to the conservation of specific angular momentum. At first glance, the fact that the size of the elliptical disk ($r \approx 1.2 \times 10^{15}$ cm) is orders of magnitude larger than R_p poses a physical problem. However, as pointed out in Holoien et al. (2019), this may be resolved if the mass of the line-emitting gas is small compared to the mass of the initial star. As such, there are several ways to transport a small amount of mass (e.g., through shocks, advection through wind, etc.) and redistribute the angular momentum quickly. We find it unlikely for the disk to spread to such a large distance through viscous processes in the observed timescale, given that the viscous timescale at the mean semimajor axis is much longer,

$$t_{\mathrm{visc}} = \alpha^{-1}(H/R)^{-2} t_{\mathrm{dyn}}$$
$$= 158 \left(\frac{\alpha}{0.1} \right)^{-1} (H/R)^{-2} \text{ days}. \qquad (3)$$

Depending on the thickness of the disk at this distance, the viscous timescale is on the order of 1–1000 years.

We can estimate the mass of the line-emitting part of the disk by considering the conservation of total angular momentum. The total angular momentum of the line-emitting region of the disk is

$$\ell_{\mathrm{disk}} = M_{\mathrm{disk}} \sqrt{GM_{\mathrm{bh}} a(1 - e^2)}$$
$$= M_{\mathrm{disk}} \sqrt{GM_{\mathrm{bh}} \xi(1 + e)}, \qquad (4)$$

where a is the semimajor axis, ξ is the pericenter distance, and e is the eccentricity. In this calculation, we evaluate the angular momentum at ξ_2. Assuming the bound stellar debris has a mass of $\sim 0.5 M_\star$, we require $\ell_{\mathrm{disk}} \lesssim 0.5 \ell_\star$. From the $\Delta t = 51$ days

observation, we find an upper limit

$$M_{\rm disk} \lesssim 0.5 M_\star \sqrt{\frac{R_{\rm p}}{\xi_2(1+e)}} = 0.04 M_\star. \qquad (5)$$

Our analysis of the Hα emission implies that the mass of the extended disk is small compared to the mass of the disrupted star and that significant transport of angular momentum has taken place in order for the disk to spread to those large distances.

Our observations show that the accretion disk in AT 2018hyz extends out to $\sim 100 R_{\rm p}$. The smooth, uniform decline in the UV and optical bands suggests no change in the dominant emission mechanism during the monitoring period and hints at the importance of accretion operating effectively in the entire duration of the TDE.

Recent numerical simulations that focus on the disk formation process have found that shocks induced by self-intersection of the debris streams are capable of redistributing angular momentum (Shiokawa et al. 2015; Bonnerot et al. 2016; Sądowski et al. 2016; Bonnerot & Lu 2020). Bonnerot & Lu (2020) found a relatively circular ($e \approx 0.2$), geometrically thick ($H/R \approx 1$) disk extending to $\sim 300 R_g$ may be achieved efficiently in $0.5 t_{\rm mb}$ (fallback time of the most-bound debris) following numerous secondary shocks generated near the self-crossing point. Within the thick disk, the gas angular momentum is sub-Keplerian, which implies that the measured line width at the same distance would be narrower than that assuming Keplerian rotation. The fact that our derived disk sizing being a few factors larger does not necessarily contradict the results from these theoretical works as we may be looking at different parts of the disk. Previous works have shown that the Hα photosphere lies near the electron scattering surface (Roth et al. 2016), which has a size of $\sim 1000 R_g$ at sight lines away from the funnel (Dai et al. 2018). The compact, puffed up TDE disk as described by Dai et al. (2018) and Bonnerot & Lu (2020) would be opaque to the Hα emission. Our observations provide evidence for the presence of a thin, nearly circular Hα-emitting disk, which may or may not be attached to a thicker disk in the center.

4.3. Non-disk Gaussian Component

Theories and observations have indicated that a radiatively driven wind may be ubiquitous among TDEs during their early phases where the debris fallback rate is thought to be "super-Eddington" (Strubbe & Quataert 2009, 2011; Alexander et al. 2016; Dai et al. 2018; Hung et al. 2019). Such a wind naturally provides a physical origin for the BLR that is likely to be responsible for the broad Gaussian component observed in AT 2018hyz and in the other optical TDEs. According to our fit, the disk component contributes half of the total Hα line flux. The Gaussian component has a FWHM of 12,000 km s^{-1} which corresponds to a virial radius of $\sim 8.9 \times 10^{14}$ cm, or $\sim 110 R_{\rm p}$ ($= 1700 R_g$), and slowly narrows ($\leqslant 30\%$) over the duration of spectroscopic monitoring. Both the line width and its lack of evolution in AT 2018hyz are similar to the broad-line emission properties of other TDEs (Figure 5).

Broad lines are also present in many AGNs and they are thought to be produced by gas above and below the disk plane at distances from light hours to light years away from the SMBH. In a TDE, the matter distribution that ensheathes the

SMBH is likely produced quickly by a wind that is supported by a combination of radiation pressure and rotation. Accretion then proceeds through the midplane. In a geometrically thin, optically thick disk, the Hα line-emitting portion of the disk corresponds to an effective temperature of about 8000 K. Changes in the properties of the disk, such as in the rate of mass supply, naturally result in changes in the line emission on an orbital timescale on the order of weeks. This is in agreement with the timescale at which the double-peak line profiles are observed to change.

4.4. Bowen Emission Lines

The appearance of the feature around 4650 Å on day 51 is either due to a blueshifted He II $\lambda 4686$ or a N III $\lambda 4641$ +He II $\lambda 4686$ emission complex. This feature persisted in all of the later spectra and provides additional evidence for ongoing accretion (Leloudas et al. 2019). In particular, the N III complex is known to be produced by the Bowen fluorescence mechanism (Bowen 1935). The mechanism can be understood as follows. First, the ionization of He II at an energy of 54.4 eV produces He II $\lambda 4686$ as well as the He II Lyα photons upon recombination. The He II Lyα line at $\lambda = 303.78$ Å has energy that is remarkably similar to the O III transitions $2p^2\ ^3P_2 - 2p3d\ ^3P_2^\circ$ and $2p^2\ ^3P_2 - 2p3d\ ^3P_1^\circ$. The radiative excitation of the O III resonance line and the subsequent cascades produce several O III lines, one of which then in turn excites the N III doublet $\lambda\lambda 374.434, 374.441$. The end result of this is the production of many O III and N III emissions in the optical wavelength range of 3000–4650 Å. Within the wavelength coverage of our spectra, we also looked for Bowen emission O III $\lambda 3760$ and N III $\lambda\lambda 4097,4104$ in our spectra. Because the N III $\lambda\lambda 4097,4104$ lines overlaps with Hγ we cannot confidently establish the detection on day 51. We note that this feature became buried in the continuum in later spectra. The O III $\lambda 3760$ line is marginally detected in the $\Delta t = 164$ days spectrum, when the He II $\lambda 4686$ complex is the strongest.

In TDEs with a low X-ray-to-optical ratio like AT 2018hyz, the observed blackbody spectrum generally could not produce enough ionizing photons to trigger the Bowen mechanism. For example, even when assuming a generous 100% energy conversion efficiency, the blackbody emission in AT 2018hyz only produces $\lesssim 10^{32}$ erg s^{-1} of luminosity below the ionization edge of He II (228 Å) and thus cannot account for the observed N III+He II luminosity of 3×10^{39} erg s^{-1}. Therefore, an additional extreme UV or X-ray source, likely an accretion disk, is required.

Van Velzen et al. (2020) classified the spectra of TDEs into three different spectral classes, namely, TDE-H , TDE-Bowen, and TDE-He that are found to be associated with distinctive rise time distributions. These three spectral classes are defined based on the species of the broad emission lines present in the spectra. The spectrum of TDE-Bowen's shows both broad He II $\lambda 4686$ and Balmer emission. TDE-H's and TDE-He's have spectra that feature only broad hydrogen and He II emission, respectively. Under this classification scheme, AT 2018hyz is shown to transition from TDE-H to TDE-Bowen in less than 2 months. The origin of this transition in spectral class in AT 2018hyz is still largely unknown yet has been reported in another TDE, ASASSN-14ae (Holoien et al. 2014; Brown et al. 2016). Brown et al. (2016) attributed this change to the hardening of the radiation field at late time. The
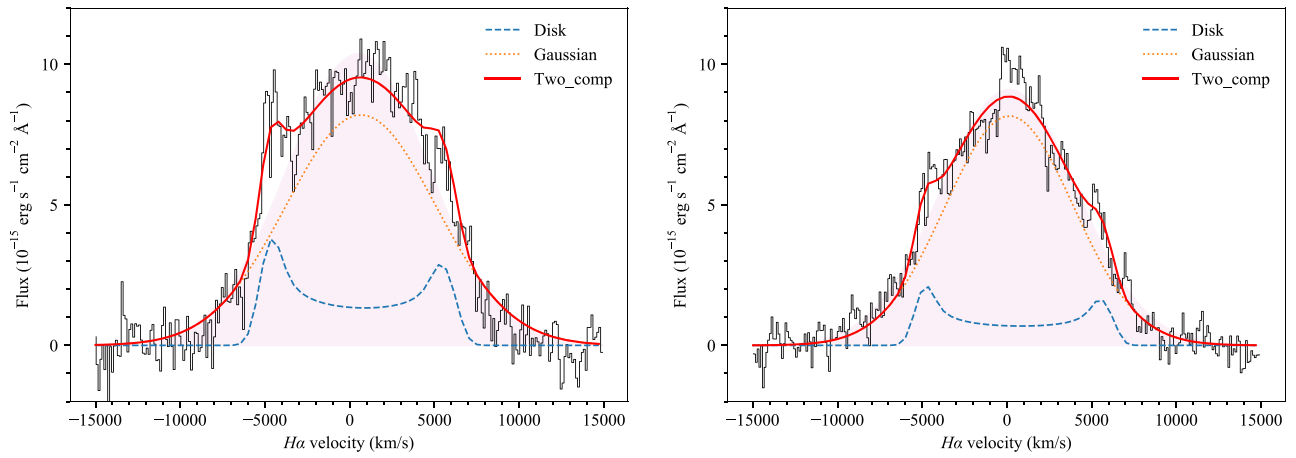
Figure 8. Best-fitting two-component models (red curves) for the Hα emission of AT 2018hyz (black curves) from the $\Delta t = 120$ days (left) and $\Delta t = 165$ days (right) spectra. The disk and Gaussian components are shown as blue and orange curves, respectively. The pink-shaded area indicates the best-fitting single-Gaussian model to the entire emission line profile, indicating that this model is insufficient at matching the peaks near $|v| = 5000$ km s^{-1}. Despite having notable disk emission, the line profile at these late phases are relatively similar to the flat-topped or single-Gaussian line profiles typically seen in TDEs.

composition of the fallback stellar material may also affect changes in the helium-to-hydrogen ratio in AT 2018hyz. Law-Smith et al. (2019) showed that the helium abundance can start to rise months after the disruption. However, we note that a detailed radiative transfer calculation, which is beyond the scope of this paper, is required to demonstrate how the change in abundance translates into the observed line ratio.

4.5. Late-time Spectroscopic Evolution

In the last spectroscopic epoch obtained on $\Delta t = 364$ days, the spectrum almost fades back to the host level. As can be seen from Figure 3, the only features in the residual spectrum is a narrow Hα emission (920 ± 60 km s^{-1}) at a systemic velocity of the host galaxy and a weak N III+He II complex (red-dashed line in Figure 5). As shown in Figure 5, it is common to see emission lines in TDE spectra narrow with time (e.g., Brown et al. 2016; Hung et al. 2017) yet not with such a significant reduction (factor of 10) in width. Comparing the Gaussian component of the spectra observed at earlier epochs shows that this change in line width suggests that the production site of Hα emission has moved from $\sim 10^{15}$ cm to $\sim 10^{17}$ cm.

A similar evolution of Hα emission at late time is seen in AT 2018zr (see the pink-dashed line in Figure 5; Hung et al. 2019). This narrow component is likely to arise from the circumnuclear gas that lies much farther out being photoionized by the TDE flare. However, since very few TDEs have spectra a year after peak brightness, we cannot yet verify whether this is trend is typical.

4.6. Double-peaked Line Profiles in TDEs

Liu et al. (2017) described a peculiar Hα emission feature in TDE PTF09djl with two peaks being separated by 3.5×10^4 km s^{-1}, suggesting it was caused by an elliptical disk with extremely high inclination and eccentricity. However, this feature was only seen in a set of three low-S/N spectra where the Hα feature falls in several telluric bands and therefore accurate continuum determination cannot be achieved. Because of these complications, PTF09djl does not show a clear and robust detection of a disk.

The derived disk properties of AT 2018hyz are also quite different from that of PTF09djl. AT 2018hyz has a fairly circular disk with a moderate-to-high inclination angle while the purported PTF09djl disk is characterized by extremely high ellipticity ($e \approx 0.97$) and a high inclination angle ($i \approx 88°$). In addition, a significant portion of the Hα-emitting disk in PTF09djl (extending from $30-400R_{\rm g}$), while the disk of AT 2018hyz locates at $1000-3000R_{\rm g}$. Our results are derived from the original Eracleous et al. (1995) prescription, which approximated photon geodesics under the weak-field limit, thus the validity of the model breaks down at $\xi < 100R_g$. We note that Liu et al. (2017) applied analytical forms of photon geodesics under a strong gravity regime, which is methodologically different from our calculation. The best-fit disk parameters presented by Liu et al. (2017) suggest that the Hα emission in PTF09djl is produced by the debris streams on highly eccentric orbits, which remained the same size for at least a duration of 2 months. Their analysis indicates that the stellar debris are unable to circularize by dissipating orbital energy.

AT 2018hyz provides a more compelling case for a disk, consistent with the classical picture where a disk forms efficiently following a TDE, though we note that recent simulations and analytical calculations have found disk formation to be inefficient in several regions of the parameter space (e.g., Dai et al. 2015; Shiokawa et al. 2015; Bonnerot et al. 2016; Hayasaki et al. 2016; Svirski et al. 2017). However, even if circularization is efficient in most TDEs, as deduced for example by the detection of Bowen emission lines in their early phases (Blagorodnova et al. 2019; Leloudas et al. 2019), double-peaked features have not been unambiguously observed in other events. It is likely that this signature is missed for configurations in which the accretion disk is less inclined, which results in them being much weaker relative to the more isotropic, broad Gaussian component (see the Hα line profiles in later epochs Figure 8). The disk of AT 2018hyz is deduced to be highly inclined with $i = 57° \pm 13$. A more face-on disk (with a lower inclination angle) may result in a more flat-topped line profile as the separation between the two peaks diminishes (e.g., the Hα emission in AT 2018zr could arise from a low-inclination disk; Holoien et al. 2019). Despite the disk contribution being weaker at later epochs for AT 2018hyz,

the disk inclination angle remains high and shows no significant precession. On the other hand, the eccentricity declines slightly, hinting that energy dissipation possibly by shocks continues to operate efficiently.

5. Conclusions

To summarize, we find that the observations of AT 2018hyz are consistent with the classical theoretical prediction in which TDE flares are powered by a newly formed accretion disk, which in turn is responsible for producing the BLR. In the context of TDE debris stream evolution, we find the first strong observational evidence for prompt circularization following the disruption of a star. This accretion is accompanied by vast amounts of energy release that results in a wide range of key elements of the flow patterns, all necessary to explain the salient properties of TDEs and are highly reminiscent of the well-studied phenomenology of steadily accreting AGN. These are an accretion disk, responsible for generating the bulk of the power, and an extended gaseous envelope, responsible for reprocessing the radiation as well as producing the broad-line features. Whereas AGN are supplied by a steady stream of fuel for thousands of years, TDEs like AT 2018hyz offer a unique opportunity to study a single SMBH under a set of conditions that vary dramatically over months. For this reason, studying objects like AT 2018hyz provide the firmest hope of understanding the physics of accretion disks around SMBHs for a wide range of accretion conditions.

Appendix

We report the X-ray flux in the 0.3–10 keV band from the Swift XRT observations in Table A1. The UV and optical photometry of AT 2018hyz is tabulated in Table A2.

Table A1
Swift XRT Observations

MJD	Integration Time (s)	Flux (10^{-14} erg s^{-1} cm^{-2})
58432.20	2420	<6.44
58434.68	2220	<6.32
58436.32	2160	<4.46
58439.58	2068	<5.97
58440.44	2562	<7.26
58442.56	2065	<8.30
58443.56	787	<9.61
58445.48	1069	<7.06
58446.41	2530	<6.77
58449.27	1788	<5.39
58453.85	2293	<6.11
58455.70	2595	6.61 ± 3.18
58458.49	2415	6.95 ± 3.14
58461.76	782	<9.65
58464.33	2080	3.95 ± 2.58
58467.53	2417	<7.39
58475.76	2475	<7.22
58481.29	2467	<7.53
58484.67	2325	<6.03
58487.66	2275	<5.81
58490.44	2312	<5.71
58493.43	2372	<8.14
58496.62	2444	<6.70
58499.41	2407	9.67 ± 3.88
58502.00	1821	<5.28
58513.10	1563	<6.77
58518.53	2010	<5.71
58521.46	1151	<9.19
58525.23	2210	<7.41
58536.54	2183	<7.50
58541.05	1573	<7.86
58545.49	2462	<6.02
58549.82	2480	<5.33
58579.09	1169	<9.06
58581.56	2467	<9.22
58584.22	1416	<8.73
58666.09	2140	<4.95

Note. XRT Flux in the 0.3–10 keV energy band is calculated from a count rate by assuming an absorbed power-law model with a photon index of $\Gamma = 2.7$ and a Galactic H I column density of 2.59×10^{20} cm^{-2}.

Table A2
Photometric Data of AT 2018hyz

MJD	Magnitude	Filter	Telescope
58432.207	16.30 ± 0.04	UVW2	Swift
58434.720	16.40 ± 0.04	UVW2	Swift
58436.326	16.49 ± 0.04	UVW2	Swift
58439.580	16.55 ± 0.04	UVW2	Swift
58440.439	16.61 ± 0.04	UVW2	Swift
58442.568	16.64 ± 0.04	UVW2	Swift
58443.561	16.59 ± 0.05	UVW2	Swift
58445.479	16.65 ± 0.05	UVW2	Swift
58446.415	16.98 ± 0.04	UVW2	Swift
58449.277	16.86 ± 0.04	UVW2	Swift
58453.853	16.92 ± 0.04	UVW2	Swift
58455.707	17.05 ± 0.04	UVW2	Swift
58458.497	17.04 ± 0.04	UVW2	Swift
58461.761	17.14 ± 0.05	UVW2	Swift
58464.337	17.25 ± 0.04	UVW2	Swift

Table A2
(Continued)

MJD	Magnitude	Filter	Telescope
58467.533	17.39 ± 0.04	UVW2	Swift
58475.764	17.49 ± 0.05	UVW2	Swift
58481.291	17.57 ± 0.05	UVW2	Swift
58484.673	17.65 ± 0.05	UVW2	Swift
58487.662	17.69 ± 0.05	UVW2	Swift
58490.438	17.72 ± 0.05	UVW2	Swift
58493.434	17.72 ± 0.05	UVW2	Swift
58496.618	17.76 ± 0.05	UVW2	Swift
58499.414	17.77 ± 0.05	UVW2	Swift
58502.000	17.83 ± 0.05	UVW2	Swift
58513.104	18.05 ± 0.06	UVW2	Swift
58518.534	17.89 ± 0.05	UVW2	Swift
58521.466	17.87 ± 0.06	UVW2	Swift
58525.235	17.90 ± 0.05	UVW2	Swift
58536.539	17.97 ± 0.05	UVW2	Swift
58541.049	18.02 ± 0.06	UVW2	Swift
58545.498	18.04 ± 0.05	UVW2	Swift
58549.819	18.06 ± 0.05	UVW2	Swift
58579.092	18.35 ± 0.07	UVW2	Swift
58581.563	18.51 ± 0.06	UVW2	Swift
58584.217	18.50 ± 0.07	UVW2	Swift
58666.093	18.97 ± 0.07	UVW2	Swift
58672.068	19.29 ± 0.07	UVW2	Swift
58432.212	15.99 ± 0.04	UVM2	Swift
58434.725	16.10 ± 0.04	UVM2	Swift
58436.331	16.15 ± 0.04	UVM2	Swift
58439.585	16.24 ± 0.04	UVM2	Swift
58440.444	16.27 ± 0.04	UVM2	Swift
58442.573	16.31 ± 0.04	UVM2	Swift
58443.564	16.38 ± 0.05	UVM2	Swift
58445.483	16.41 ± 0.04	UVM2	Swift
58446.419	16.61 ± 0.04	UVM2	Swift
58449.281	16.56 ± 0.04	UVM2	Swift
58453.857	16.71 ± 0.04	UVM2	Swift
58455.712	16.81 ± 0.04	UVM2	Swift
58458.502	16.87 ± 0.04	UVM2	Swift
58461.764	16.97 ± 0.05	UVM2	Swift
58464.340	17.06 ± 0.04	UVM2	Swift
58467.537	17.18 ± 0.04	UVM2	Swift
58475.770	17.41 ± 0.05	UVM2	Swift
58481.294	17.57 ± 0.05	UVM2	Swift
58484.679	17.56 ± 0.05	UVM2	Swift
58487.666	17.65 ± 0.05	UVM2	Swift
58490.441	17.61 ± 0.05	UVM2	Swift
58493.437	17.70 ± 0.05	UVM2	Swift
58496.622	17.71 ± 0.05	UVM2	Swift
58499.418	17.70 ± 0.05	UVM2	Swift
58502.004	17.79 ± 0.05	UVM2	Swift
58513.625	17.99 ± 0.06	UVM2	Swift
58518.538	17.83 ± 0.05	UVM2	Swift
58521.468	17.91 ± 0.06	UVM2	Swift
58525.238	17.87 ± 0.05	UVM2	Swift
58536.542	18.03 ± 0.05	UVM2	Swift
58541.056	17.98 ± 0.06	UVM2	Swift
58545.505	18.17 ± 0.05	UVM2	Swift
58549.823	18.15 ± 0.05	UVM2	Swift
58579.095	18.44 ± 0.08	UVM2	Swift
58581.567	18.60 ± 0.06	UVM2	Swift
58584.219	18.67 ± 0.07	UVM2	Swift
58666.097	19.23 ± 0.08	UVM2	Swift
58672.072	19.45 ± 0.08	UVM2	Swift
58432.203	15.99 ± 0.04	UVW1	Swift
58434.676	16.02 ± 0.04	UVW1	Swift
58436.322	16.07 ± 0.04	UVW1	Swift

Table A2
(Continued)

MJD	Magnitude	Filter	Telescope
58439.576	16.18 ± 0.04	UVW1	Swift
58440.435	16.23 ± 0.04	UVW1	Swift
58442.564	16.24 ± 0.04	UVW1	Swift
58443.559	16.29 ± 0.05	UVW1	Swift
58445.476	16.35 ± 0.05	UVW1	Swift
58446.411	16.47 ± 0.04	UVW1	Swift
58449.274	16.41 ± 0.04	UVW1	Swift
58453.850	16.53 ± 0.04	UVW1	Swift
58455.703	16.65 ± 0.04	UVW1	Swift
58458.492	16.77 ± 0.04	UVW1	Swift
58461.758	16.82 ± 0.06	UVW1	Swift
58464.334	16.96 ± 0.05	UVW1	Swift
58467.530	17.04 ± 0.05	UVW1	Swift
58475.758	17.24 ± 0.05	UVW1	Swift
58481.289	17.31 ± 0.05	UVW1	Swift
58484.669	17.46 ± 0.05	UVW1	Swift
58487.658	17.36 ± 0.05	UVW1	Swift
58490.436	17.44 ± 0.05	UVW1	Swift
58493.431	17.49 ± 0.05	UVW1	Swift
58496.616	17.51 ± 0.05	UVW1	Swift
58499.410	17.52 ± 0.05	UVW1	Swift
58501.997	17.53 ± 0.06	UVW1	Swift
58513.102	17.78 ± 0.06	UVW1	Swift
58518.531	17.66 ± 0.06	UVW1	Swift
58521.464	17.77 ± 0.07	UVW1	Swift
58525.232	17.71 ± 0.06	UVW1	Swift
58536.537	17.80 ± 0.06	UVW1	Swift
58541.044	17.86 ± 0.06	UVW1	Swift
58545.493	17.99 ± 0.06	UVW1	Swift
58549.815	18.03 ± 0.06	UVW1	Swift
58579.090	18.33 ± 0.08	UVW1	Swift
58581.560	18.51 ± 0.07	UVW1	Swift
58584.215	18.47 ± 0.08	UVW1	Swift
58666.090	18.84 ± 0.09	UVW1	Swift
58672.064	19.11 ± 0.10	UVW1	Swift
58432.205	16.08 ± 0.04	U	Swift
58434.678	15.96 ± 0.04	U	Swift
58436.325	16.13 ± 0.04	U	Swift
58439.578	16.16 ± 0.04	U	Swift
58440.437	16.17 ± 0.04	U	Swift
58442.566	16.19 ± 0.04	U	Swift
58443.560	16.16 ± 0.06	U	Swift
58445.478	16.22 ± 0.05	U	Swift
58446.413	16.30 ± 0.04	U	Swift
58449.276	16.31 ± 0.04	U	Swift
58453.852	16.45 ± 0.04	U	Swift
58455.705	16.50 ± 0.04	U	Swift
58458.495	16.57 ± 0.04	U	Swift
58461.760	16.66 ± 0.07	U	Swift
58464.336	16.72 ± 0.05	U	Swift
58467.532	16.84 ± 0.05	U	Swift
58475.762	16.97 ± 0.05	U	Swift
58481.290	17.04 ± 0.05	U	Swift
58484.672	17.17 ± 0.05	U	Swift
58487.660	17.27 ± 0.05	U	Swift
58490.437	17.24 ± 0.05	U	Swift
58493.432	17.32 ± 0.05	U	Swift
58496.617	17.35 ± 0.05	U	Swift
58499.412	17.32 ± 0.05	U	Swift
58501.999	17.43 ± 0.06	U	Swift
58513.104	17.56 ± 0.07	U	Swift
58518.533	17.42 ± 0.06	U	Swift
58521.465	17.54 ± 0.08	U	Swift
58525.234	17.57 ± 0.06	U	Swift

Table A2
(Continued)

MJD	Magnitude	Filter	Telescope
58536.538	17.69 ± 0.06	U	Swift
58541.047	17.91 ± 0.08	U	Swift
58545.496	17.77 ± 0.06	U	Swift
58549.817	17.88 ± 0.07	U	Swift
58579.091	18.23 ± 0.10	U	Swift
58581.562	18.34 ± 0.08	U	Swift
58584.216	18.16 ± 0.09	U	Swift
58666.092	18.50 ± 0.11	U	Swift
58672.067	18.59 ± 0.11	U	Swift
58438.328	16.29 ± 0.01	g	Swope
58440.331	16.25 ± 0.01	g	Swope
58442.343	16.29 ± 0.01	g	Swope
58443.325	16.32 ± 0.01	g	Swope
58449.331	16.45 ± 0.01	g	Swope
58451.335	16.54 ± 0.01	g	Swope
58460.311	16.68 ± 0.01	g	Swope
58463.319	16.69 ± 0.01	g	Swope
58466.290	16.76 ± 0.01	g	Swope
58468.297	16.70 ± 0.01	g	Swope
58471.275	16.91 ± 0.01	g	Swope
58474.345	16.95 ± 0.01	g	Swope
58480.306	17.12 ± 0.01	g	Swope
58484.357	17.10 ± 0.01	g	Swope
58487.336	17.10 ± 0.01	g	Swope
58491.339	17.14 ± 0.01	g	Swope
58494.294	17.21 ± 0.02	g	Swope
58498.203	17.29 ± 0.01	g	Swope
58511.269	17.42 ± 0.02	g	Swope
58514.230	17.37 ± 0.01	g	Swope
58519.346	17.46 ± 0.01	g	Swope
58521.206	17.47 ± 0.01	g	Swope
58525.338	17.38 ± 0.01	g	Swope
58528.392	17.68 ± 0.02	g	Swope
58540.291	17.70 ± 0.01	g	Swope
58544.102	17.67 ± 0.01	g	Swope
58551.224	17.65 ± 0.01	g	Swope
58556.136	17.89 ± 0.01	g	Swope
58559.232	17.88 ± 0.01	g	Swope
58571.080	17.87 ± 0.01	g	Swope
58579.176	17.93 ± 0.01	g	Swope
58585.122	17.98 ± 0.01	g	Swope
58588.069	18.02 ± 0.01	g	Swope
58600.036	18.14 ± 0.02	g	Swope
58609.010	18.40 ± 0.01	g	Swope
58616.073	18.42 ± 0.01	g	Swope
58637.040	18.42 ± 0.01	g	Swope
58643.007	18.16 ± 0.01	g	Swope
58659.976	18.20 ± 0.01	g	Swope
58674.970	18.57 ± 0.04	g	Swope
58438.321	16.56 ± 0.00	r	Swope
58440.323	16.49 ± 0.00	r	Swope
58442.350	16.56 ± 0.00	r	Swope
58443.317	16.53 ± 0.01	r	Swope
58447.321	16.61 ± 0.01	r	Swope
58449.339	16.63 ± 0.01	r	Swope
58451.328	16.68 ± 0.01	r	Swope
58460.319	16.90 ± 0.01	r	Swope
58463.312	16.91 ± 0.01	r	Swope
58466.297	16.98 ± 0.01	r	Swope
58468.291	17.02 ± 0.01	r	Swope
58471.282	17.10 ± 0.01	r	Swope
58474.339	17.16 ± 0.01	r	Swope
58480.299	17.37 ± 0.01	r	Swope

Table A2
(Continued)

MJD	Magnitude	Filter	Telescope
58484.352	17.38 ± 0.01	r	Swope
58487.329	17.44 ± 0.01	r	Swope
58491.332	17.49 ± 0.01	r	Swope
58494.287	17.56 ± 0.01	r	Swope
58498.195	17.66 ± 0.01	r	Swope
58511.262	17.85 ± 0.01	r	Swope
58514.223	17.88 ± 0.01	r	Swope
58519.354	18.08 ± 0.01	r	Swope
58521.194	17.94 ± 0.01	r	Swope
58525.349	18.05 ± 0.02	r	Swope
58527.380	18.13 ± 0.01	r	Swope
58540.280	18.34 ± 0.01	r	Swope
58544.113	18.29 ± 0.01	r	Swope
58551.204	18.45 ± 0.01	r	Swope
58556.122	18.59 ± 0.01	r	Swope
58559.216	18.71 ± 0.01	r	Swope
58571.065	18.86 ± 0.01	r	Swope
58579.161	18.98 ± 0.01	r	Swope
58585.139	19.08 ± 0.01	r	Swope
58588.054	18.95 ± 0.02	r	Swope
58600.020	19.28 ± 0.02	r	Swope
58608.994	19.39 ± 0.08	r	Swope
58608.995	19.33 ± 0.02	r	Swope
58616.057	19.59 ± 0.03	r	Swope
58637.025	19.61 ± 0.02	r	Swope
58642.984	19.68 ± 0.04	r	Swope
58642.992	19.37 ± 0.02	r	Swope
58659.961	19.60 ± 0.03	r	Swope
58438.324	16.63 ± 0.00	i	Swope
58440.327	16.56 ± 0.00	i	Swope
58442.347	16.58 ± 0.00	i	Swope
58443.321	16.58 ± 0.01	i	Swope
58447.326	16.64 ± 0.01	i	Swope
58449.335	16.63 ± 0.00	i	Swope
58451.331	16.71 ± 0.01	i	Swope
58460.315	16.87 ± 0.01	i	Swope
58463.315	16.88 ± 0.00	i	Swope
58466.294	16.96 ± 0.01	i	Swope
58468.294	17.02 ± 0.01	i	Swope
58471.279	17.07 ± 0.01	i	Swope
58474.342	17.07 ± 0.01	i	Swope
58480.302	17.33 ± 0.01	i	Swope
58487.332	17.41 ± 0.01	i	Swope
58491.336	17.44 ± 0.01	i	Swope
58494.290	17.50 ± 0.01	i	Swope
58498.199	17.63 ± 0.01	i	Swope
58511.266	17.83 ± 0.01	i	Swope
58514.226	17.85 ± 0.01	i	Swope
58519.350	18.07 ± 0.01	i	Swope
58521.200	17.98 ± 0.01	i	Swope
58525.344	18.18 ± 0.02	i	Swope
58527.386	18.18 ± 0.03	i	Swope
58540.286	18.34 ± 0.01	i	Swope
58551.211	18.48 ± 0.01	i	Swope
58551.218	18.48 ± 0.01	i	Swope
58559.224	18.74 ± 0.02	i	Swope
58571.073	18.80 ± 0.01	i	Swope
58579.169	18.87 ± 0.02	i	Swope
58585.131	19.08 ± 0.02	i	Swope
58588.062	18.91 ± 0.02	i	Swope
58600.028	19.28 ± 0.02	i	Swope

Table A2
(Continued)

MJD	Magnitude	Filter	Telescope
58616.065	19.50 ± 0.03	i	Swope
58637.033	19.58 ± 0.03	i	Swope
58659.968	19.79 ± 0.04	i	Swope

Note. All the data presented in this table have been Galactic extinction corrected. We did not perform host subtraction on the Swift UV data since the host contribution is negligible. On the other hand, the Swope data are host subtracted.

ORCID iDs

Tiara Hung ⓘ https://orcid.org/0000-0002-9878-7889
Enrico Ramirez-Ruiz ⓘ https://orcid.org/0000-0003-2558-3102
Katie Auchettl ⓘ https://orcid.org/0000-0002-4449-9152
Charles D. Kilpatrick ⓘ https://orcid.org/0000-0002-5740-7747
Brenna Mockler ⓘ https://orcid.org/0000-0001-6350-8168
Jonathan S. Brown ⓘ https://orcid.org/0000-0002-1885-6419
David A. Coulter ⓘ https://orcid.org/0000-0003-4263-2228
Georgios Dimitriadis ⓘ https://orcid.org/0000-0001-9494-179X
Thomas W.-S. Holoien ⓘ https://orcid.org/0000-0001-9206-3460
Jamie A. P. Law-Smith ⓘ https://orcid.org/0000-0001-8825-4790
Anthony L. Piro ⓘ https://orcid.org/0000-0001-6806-0673

References

Aihara, H., Allende Prieto, C., An, D., et al. 2011, ApJS, 193, 29
Alexander, K. D., Berger, E., Guillochon, J., Zauderer, B. A., & Williams, P. K. G. 2016, ApJL, 819, L25
Arcavi, I., Gal-Yam, A., Sullivan, M., et al. 2014, ApJ, 793, 38
Arnaud, K. A. 1996, in ASP Conf. Ser. 101, Astronomical Data Analysis Software and Systems V, ed. G. H. Jacoby & J. Barnes (San Francisco, CA: ASP), 17
Auchettl, K., Guillochon, J., & Ramirez-Ruiz, E. 2017, ApJ, 838, 149
Becker, A. 2015, HOTPANTS: High Order Transform of PSF ANd Template Subtraction, Astrophysics Source Code Library, ascl:1504.004
Bennett, C. L., Larson, D., Weiland, J. L., et al. 2013, ApJS, 208, 20
Blagorodnova, N., Cenko, S. B., Kulkarni, S. R., et al. 2019, ApJ, 873, 92
Blagorodnova, N., Gezari, S., Hung, T., et al. 2017, ApJ, 844, 46
Blanchard, P. K., Nicholl, M., Berger, E., et al. 2017, ApJ, 843, 106
Bonnerot, C., & Lu, W. 2020, MNRAS, 495, 1374
Bonnerot, C., Rossi, E. M., & Lodato, G. 2017, MNRAS, 464, 2816
Bonnerot, C., Rossi, E. M., Lodato, G., & Price, D. J. 2016, MNRAS, 455, 2253
Bouvier, J. 2013, in EAS Publ. Ser. 62, Role and Mechanisms of Angular Momentum Transport During the Formation and Early Evolution of Stars, Evry Schatzman School 2012, ed. P. Hennebelle & C. Charbonnel (Les Ulis: EDP Sciences), 143
Bowen, I. S. 1935, ApJ, 81, 1
Brown, J. S., Holoien, T. W.-S., Auchettl, K., et al. 2017, MNRAS, 466, 4904
Brown, J. S., Shappee, B. J., Holoien, T. W.-S., et al. 2016, MNRAS, 462, 3993
Cardelli, J. A., Clayton, G. C., & Mathis, J. S. 1989, ApJ, 345, 245
Chen, K., Halpern, J. P., & Filippenko, A. V. 1989, ApJ, 339, 742
Choi, J., Dotter, A., Conroy, C., et al. 2016, ApJ, 823, 102
Clemens, J. C., Crain, J. A., & Anderson, R. 2004, Proc. SPIE, 5492, 331
Cutri, R. M., Skrutskie, M. F., van Dyk, S., et al. 2003, The IRSA 2MASS All-Sky Point Source Catalog, NASA/IPAC Infrared Science Archive, http://irsa.ipac.caltech.edu/applications/Gator/
Dai, L., Escala, A., & Coppi, P. 2013, ApJL, 775, L9
Dai, L., McKinney, J. C., & Miller, M. C. 2015, ApJL, 812, L39
Dai, L., McKinney, J. C., Roth, N., Ramirez-Ruiz, E., & Miller, M. C. 2018, ApJL, 859, L20
Dimitriadis, G., Rojas-Bravo, C., Kilpatrick, C. D., et al. 2019, ApJL, 870, L14
Dong, S., Bose, S., Chen, P., et al. 2018, ATel, 12198, 1
Dotter, A. 2016, ApJS, 222, 8
Eracleous, M., Livio, M., Halpern, J. P., & Storchi-Bergmann, T. 1995, ApJ, 438, 610
Flewelling, H. A., Magnier, E. A., Chambers, K. C., et al. 2016, arXiv:1612.05243

Foley, R. J., Papenkova, M. S., Swift, B. J., et al. 2003, PASP, 115, 1220
Foreman-Mackey, D., Hogg, D. W., Lang, D., & Goodman, J. 2013, PASP, 125, 306
Frank, J., & Rees, M. J. 1976, MNRAS, 176, 633
French, K. D., Arcavi, I., & Zabludoff, A. 2016, ApJL, 818, L21
Gafton, E., & Rosswog, S. 2019, MNRAS, 487, 4790
Gehrels, N., Chincarini, G., Giommi, P., et al. 2004, ApJ, 611, 1005
Gezari, S., Cenko, S. B., & Arcavi, I. 2017, ApJL, 851, L47
Gezari, S., Chornock, R., Rest, A., et al. 2012, Natur, 485, 217
Golightly, E. C. A., Coughlin, E. R., & Nixon, C. J. 2019, ApJ, 872, 163
Gomez, S., Nicholl, M., Short, P., et al. 2020, MNRAS, 497, 1925
Graur, O., French, K. D., Zahid, H. J., et al. 2018, ApJ, 853, 39
Guillochon, J., Manukian, H., & Ramirez-Ruiz, E. 2014, ApJ, 783, 23
Guillochon, J., Nicholl, M., Villar, V. A., et al. 2018, ApJS, 236, 6
Guillochon, J., & Ramirez-Ruiz, E. 2013, ApJ, 767, 25
Guillochon, J., & Ramirez-Ruiz, E. 2015, ApJ, 809, 166
Hayasaki, K., Saito, H., & Mineshige, S. 2013, PASJ, 65, 86
Hayasaki, K., Stone, N., & Loeb, A. 2016, MNRAS, 461, 3760
Hills, J. G. 1975, Natur, 254, 295
HI4PI Collaboration, Ben Bekhti, N., Flöer, L., et al. 2016, A&A, 594, A116
Holoien, T. W.-S., Huber, M. E., Shappee, B. J., et al. 2019, ApJ, 880, 120
Holoien, T. W.-S., Kochanek, C. S., Prieto, J. L., et al. 2016a, MNRAS, 455, 2918
Holoien, T. W.-S., Kochanek, C. S., Prieto, J. L., et al. 2016b, MNRAS, 463, 3813
Holoien, T. W.-S., Prieto, J. L., Bersier, D., et al. 2014, MNRAS, 445, 3263
Horesh, A., Sfaradi, I., Bright, J., & Fender, R. 2018, ATel, 12218, 1
Horne, K., & Saar, S. H. 1991, ApJL, 374, L55
Hung, T., Cenko, S. B., Roth, N., et al. 2019, ApJ, 879, 119
Hung, T., Gezari, S., Blagorodnova, N., et al. 2017, ApJ, 842, 29
Jiang, Y.-F., Guillochon, J., & Loeb, A. 2016, ApJ, 830, 125
Kara, E., Dai, L., Reynolds, C. S., & Kallman, T. 2018, MNRAS, 474, 3593
King, A. R., & Pounds, K. A. 2003, MNRAS, 345, 657
Law-Smith, J., Guillochon, J., & Ramirez-Ruiz, E. 2019, ApJL, 882, L25
Law-Smith, J., Ramirez-Ruiz, E., Ellison, S. L., & Foley, R. J. 2017, ApJ, 850, 22
Leloudas, G., Dai, L., Arcavi, I., et al. 2019, ApJ, 887, 218
Liu, F. K., Zhou, Z. Q., Cao, R., Ho, L. C., & Komossa, S. 2017, MNRAS, 472, L99
Lodato, G., & Rossi, E. M. 2011, MNRAS, 410, 359
Loeb, A., & Ulmer, A. 1997, ApJ, 489, 573
Lu, W., & Bonnerot, C. 2020, MNRAS, 492, 686
McConnell, N. J., & Ma, C.-P. 2013, ApJ, 764, 184

Miller, J. M., Kaastra, J. S., Miller, M. C., et al. 2015, Natur, 526, 542
Miller, J. S., & Stone, R. P. S. 1993, Lick Observatory Technical Report, 66
Mockler, B., Guillochon, J., & Ramirez-Ruiz, E. 2019, ApJ, 872, 151
Moretti, A., Campana, S., Tagliaferri, G., et al. 2004, Proc. SPIE, 5165, 232
Ohsuga, K., Mori, M., Nakamoto, T., & Mineshige, S. 2005, ApJ, 628, 368
Oke, J. B., Cohen, J. G., Carr, M., et al. 1995, PASP, 107, 375
Paxton, B., Bildsten, L., Dotter, A., et al. 2011, ApJS, 192, 3
Paxton, B., Cantiello, M., Arras, P., et al. 2013, ApJS, 208, 4
Paxton, B., Marchant, P., Schwab, J., et al. 2015, ApJS, 220, 15
Piran, T., Svirski, G., Krolik, J., Cheng, R. M., & Shiokawa, H. 2015, ApJ, 806, 164
Ramirez-Ruiz, E., & Rosswog, S. 2009, ApJL, 697, L77
Rees, M. J. 1988, Natur, 333, 523
Rest, A., Scolnic, D., Foley, R. J., et al. 2014, ApJ, 795, 44
Rest, A., Stubbs, C., Becker, A. C., et al. 2005, ApJ, 634, 1103
Roming, P. W. A., Kennedy, T. E., Mason, K. O., et al. 2005, SSRv, 120, 95
Roth, N., & Kasen, D. 2018, ApJ, 855, 54
Roth, N., Kasen, D., Guillochon, J., & Ramirez-Ruiz, E. 2016, ApJ, 827, 3
Sądowski, A., Tejeda, E., Gafton, E., Rosswog, S., & Abarca, D. 2016, MNRAS, 458, 4250
Schechter, P. L., Mateo, M., & Saha, A. 1993, PASP, 105, 1342
Schlafly, E. F., & Finkbeiner, D. P. 2011, ApJ, 737, 103
Science Software Branch at STScI 2012, PyRAF: Python alternative for IRAF, Astrophysics Source Code Library, ascl:1207.011
Scolnic, D., Casertano, S., Riess, A., et al. 2015, ApJ, 815, 117
Shakura, N. I., & Sunyaev, R. A. 1973, A&A, 24, 337
Shappee, B. J., Prieto, J. L., Grupe, D., et al. 2014, ApJ, 788, 48
Shiokawa, H., Krolik, J. H., Cheng, R. M., Piran, T., & Noble, S. C. 2015, ApJ, 804, 85
Short, P., Nicholl, M., Lawrence, A., et al. 2020, MNRAS, 498, 4119
Silverman, J. M., Foley, R. J., Filippenko, A. V., et al. 2012, MNRAS, 425, 1789
Strateva, I. V., Strauss, M. A., Hao, L., et al. 2003, AJ, 126, 1720
Strubbe, L. E., & Quataert, E. 2009, MNRAS, 400, 2070
Strubbe, L. E., & Quataert, E. 2011, MNRAS, 415, 168
Svirski, G., Piran, T., & Krolik, J. 2017, MNRAS, 467, 1426
van Velzen, S., Gezari, S., Cenko, S. B., et al. 2019, ApJ, 872, 198
van Velzen, S., Gezari, S., Hammerstein, E., et al. 2020, arXiv:2001.01409
Wevers, T., van Velzen, S., Jonker, P. G., et al. 2017, MNRAS, 471, 1694
Wilkins, D. R., & Fabian, A. C. 2012, MNRAS, 424, 1284
Williams, R. E. 1980, ApJ, 235, 939
Xiao, T., Barth, A. J., Greene, J. E., et al. 2011, ApJ, 739, 28